Nagaoka ferromagnetism observed in a quantum dot plaquette

Juan P. Dehollain,[1,*] Uditendu Mukhopadhyay,[1,*] Vincent P. Michal,[1] Yao Wang,[2] Bernhard Wunsch,[2] Christian Reichl,[3] Werner Wegscheider,[3] Mark S. Rudner,[4] Eugene Demler,[2] and Lieven M.K. Vandersypen[1,†]

[1] *QuTech and Kavli Institute of Nanoscience, TU Delft, 2600 GA Delft, The Netherlands*
[2] *Department of Physics, Harvard University, Cambridge 02138, USA*
[3] *Solid State Physics Laboratory, ETH Zürich, Zürich 8093, Switzerland*
[4] *Center for Quantum Devices and Niels Bohr International Academy, Niels Bohr Institute, University of Copenhagen, 2100 Copenhagen, Denmark*

The analytical tractability of Nagaoka ferromagnetism makes it a convenient model to explore the capabilities of quantum simulators of collective electron interactions. However, the small ground-to-excited state energy compared to electron interactions, as well as the difficulty of measuring magnetization in few particle devices, have made the Nagaoka model experimentally unattainable. Here we present experimental signatures of the ferromagnetic ground state, predicted for 3 electrons in a 4 site square plaquette, engineered using electrostatically defined quantum dots. We test the robustness of the Nagaoka condition under different scenarios of lattice topology, device homogeneity and magnetic flux through the plaquette. This long-sought demonstration of Nagaoka ferromagnetism establishes quantum dot systems as prime candidates for quantum simulators of magnetic phenomena driven by electron-electron interactions.

INTRODUCTION

The emergence of magnetism in itinerant electron systems presents a fascinating and challenging problem at the heart of quantum many-body physics [1, 2]. This may sound surprising since the most common ferromagnetic material–iron–is a metal. However, in iron, as well as many other materials including cobalt, nickel, manganite materials, magnetism is dominated by spins of nearly localized electrons, with conduction band electrons providing indirect exchange interactions. Going back to Stoner [3], simple models have been introduced to provide simple theoretical models for itinerant ferromagnetism. Here, magnetism must emerge from a delicate quantum mechanical interplay between the potential energy that can be saved through building appropriate symmetries and correlations into electronic wave functions, and the corresponding costs in kinetic energy. Despite their simplicity, the existence of ferromagnetic phases in these models remains a subject of considerable controversy [4]. The most recent experimental effort towards observing a ferromagnetic instability in itinerant Fermi systems has been undertaken with ultracold atoms [5], although the interpretation of those experiments has evolved in time [6]. On the theory side, there are only few rigorous theoretical results for itinerant magnetism, for instance in systems with special flat bands and Nagaoka's ferromagnetism (see Ref. [7] and references therein).

The Nagaoka model of ferromagnetism [8] relies on the simplicity of the Hubbard model [9], which captures complex correlations between electrons in a lattice using only two Hamiltonian parameters. Using this single-band model, Nagaoka proved analytically that for some lattice configurations and in the limit of very strong interactions, the presence of a single hole on top of a Mott insulating state with one electron per site renders the ground state ferromagnetic.

This elegant theoretical demonstration of ferromagnetism in the Hubbard model poses the question whether the ferromagnetic ground state will persist in an experimental setting, in the presence of long-range interactions and disorder, as well as additional available orbitals. The feasibility of performing a quantum simulation of Nagaoka ferromagnetism has been explored for quantum dots [10–12] as well as optical superlattices [13]. In spite of the maturity of quantum simulations of the Hubbard model, led by the cold atoms community [14], there has been no experimental observation of a high-spin ground state in an almost half-filled lattice or array of itinerant electrons–the smoking gun of Nagaoka ferromagnetism.

Electrostatically defined semiconductor quantum dots [15–17] have been gaining attention as excellent candidates for quantum simulations of the Hubbard model [18, 19]. Recent results have demonstrated the feasibility to extend these systems into 2D lattices [20–24]. The ability to reach interesting interaction regimes along with low temperatures, as well as the ability to perform spin correlation measurements, make quantum dot arrays particularly appealing for overcoming the challenges of observing evidence of Nagaoka ferromagnetism.

In this article, we present experimental signatures of Nagaoka ferromagnetism, using a quantum dot device designed to host a 2×2 lattice of electrons [23]. Using the high degree of parameter tunability, we study how external magnetic fields and disorder in local potentials affect the ferromagnetic ground state. Furthermore, by effectively tuning the geometry of the system from periodic to open boundary conditions, we experimentally demonstrate the suppression of magnetism expected from the Lieb-Mattis theorem [25].

* These authors contributed equally to this work.
† Corresponding author. Email: l.m.k.vandersypen@tudelft.nl

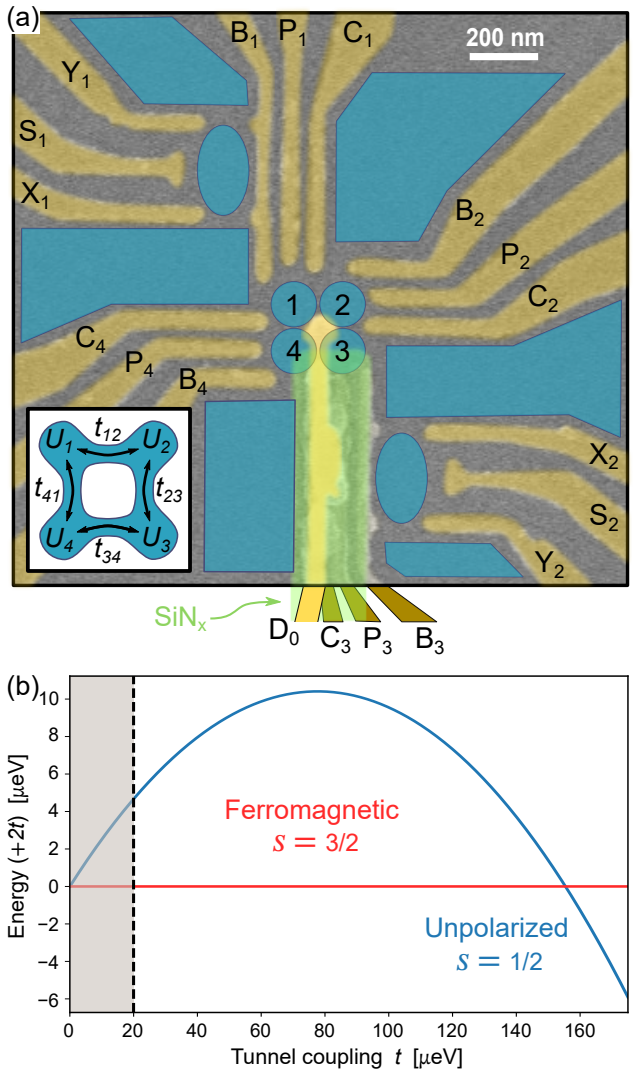

FIG. 1. (a) False colored SEM image of a device from the same batch as the one used in the experiments. The gate structure used to define the quantum dots is colored in dark gold. A slab of silicon nitride (colored in green) is laid over gates C_3 and P_3, to electrically isolate those gates from the D_0 gate (colored in bright gold) which runs over them and contacts the substrate at the center of the structure. A sketch of the expected 2DEG density in blue shows the 4 dots forming a plaquette in the center of the device, along with nearby charge sensors and electron reservoirs. (b) Energy spectrum as a function of tunnel coupling using the solution expressed in Eq. 2, with $U = 2.9$ meV. Shaded area shows the experimentally accessible range of t in this system.

NAGAOKA MODEL IN THE QUANTUM DOT PLAQUETTE

The single-band Hubbard model provides a simple description of interacting electrons in a lattice, through a Hamiltonian that contains competing kinetic energy and electron-electron interaction terms:

$$\mathcal{H}_H = -\sum_{\langle i,j\rangle\sigma} t_{i,j} c^\dagger_{i\sigma} c_{j\sigma} + \sum_i U_i n_{i\uparrow} n_{i\downarrow} - \sum_i \mu_i n_i, \quad (1)$$

where $t_{i,j}$ is the matrix element accounting for electron tunneling between sites i and j, U_i is the on-site Coulomb repulsion energy on site i and μ_i is a local energy offset at dot i, which can be electrostatically controlled. The operators $c_{i\sigma}$, $c^\dagger_{i\sigma}$ and $n_{i\sigma}$ represent the second quantization annihilation, creation and number operators for an electron on site i with spin projection $\sigma = \{\uparrow, \downarrow\}$.

To study the conditions under which Nagaoka ferromagnetism can manifest itself on a square plaquette, we restrict the system to 3 electrons (i.e. one less than half filling), with nearest-neighbor only coupling and periodic boundary conditions (see schematic in inset of Fig. 1a). This case is analytically solvable [10] for homogeneous interactions ($U_i = U$, $t_{i,j} = t$, $\mu_i = 0$) and in the limit $U \gg t$, where the eigenstates have energies:

$$E_{3/2} = -2t \quad \text{and} \quad E_{1/2} = -\sqrt{3}t - \frac{5t^2}{U}, \quad (2)$$

where $E_{3/2}$ is the energy of the ferromagnetic quadruplets (with total spin $s = 3/2$ and spin projections $m = \{\pm 1/2, \pm 3/2\}$) and $E_{1/2}$ is the energy of the 2 sets of low-spin $s = 1/2$ doublets, which are degenerate in this model [26].

The simple Hamiltonian in Eq. 1 does not account for some of the essential features of the experimental device. For comparison with experimental results, we employ a more general model Hamiltonian, in which we account for interdot Coulomb repulsion (in Fig. 2a), spin-orbit and hyperfine interactions (in Fig. 3b), as well as the effects of external magnetic fields (in Fig. 5a-b). The implementation of these terms is described in detail in the supplementary text. In addition to this model, we have also performed an ab initio calculation [26] based on multiple orbitals solved from a potential landscape with 2×2 minima, showing very similar results to those obtained with Eq. 1.

EXPERIMENTAL ACCESS TO THE NAGAOKA REGIME

The quantum dot plaquette (Fig. 1a) is formed by biasing metallic gates patterned on top of an AlGaAs/GaAs heterostructure, to control the local density of a 2-dimensional electron gas (2DEG) located 90 nm below the surface of the substrate. We use two additional nearby dots as charge sensors, to measure charge stability diagrams where we can observe charge tunneling events either between an electron reservoir and a dot, or between two dots in the plaquette. These diagrams (such as the one in Fig. 2a) allow us to map out the charge occupation of the system, as a function of voltage in the gates. The device is tuned to a regime where the system

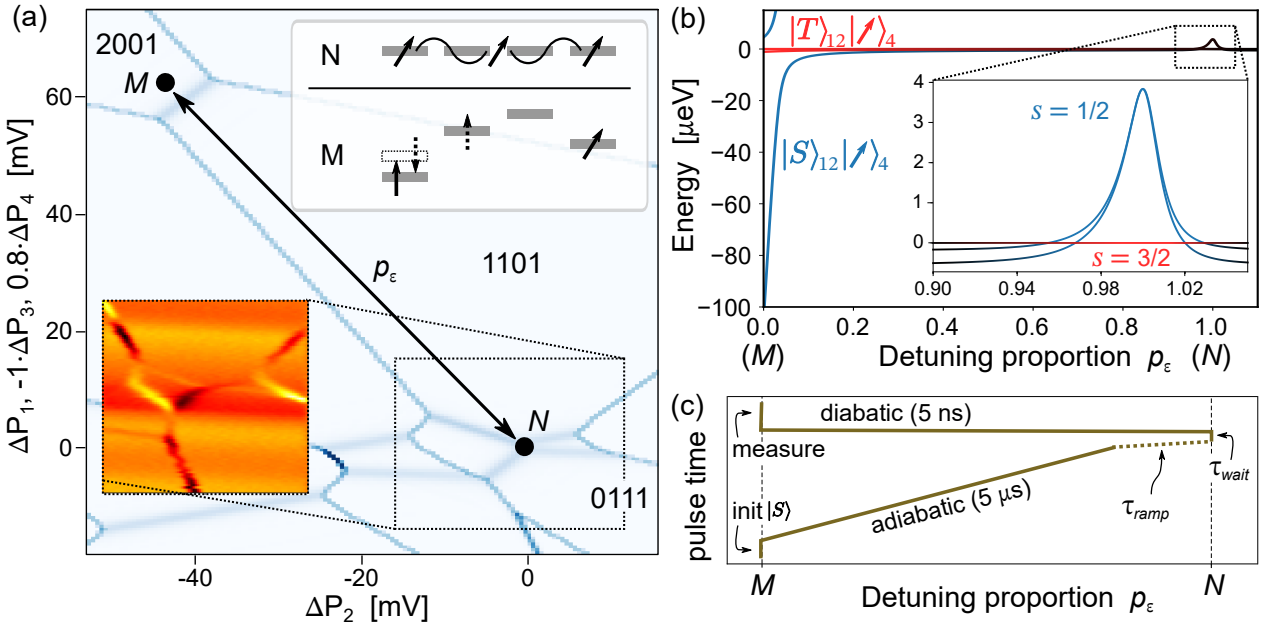

FIG. 2. (a) Simulated charge stability diagram showing the approximate gate space used in the experiment. In the experiment we pulse in a straight line in gate space from point M to point N and back. Top-right inset shows a schematic of the local energies at points N and M, highlighting in the latter how the measurement of 2 spins in the singlet-triplet basis is performed through spin-to-charge conversion. Lower-left inset shows a measured charge stability diagram of the dotted region, with the same gate voltage ratios as the simulation, which we use in the experiment to calibrate the gate voltages at point N. (b) Calculated energy spectrum as a function of detuning proportion, using the theoretical model (Eq. 1 and supplementary text) without spin-coupling effects. Parameter values were set to $U_i = [2.9, 2.6, 2.9, 3.0]$ meV and $t_{i,j} = 16$ μeV, as extracted from the experiment. Inset shows a zoomed-in spectrum of the region where the 3 spins are delocalized on all 4 dots, where there are a total of 8 states: the $s = 3/2$ quadruplets (red) and the 2 sets of $s = 1/2$ doublets (blue), of which one set connects with the $|T\rangle$ branch and the other with the $|S\rangle$ branch at point M. Line colors represent the spin state of the system in each region, denoted by the labels in the figure. The energies extracted from the numerical solutions are offset by the energy of $|s, m\rangle = |3/2, +3/2\rangle$. (c) Pulse sequence used in the experiment (see main text for detailed description).

is loaded with 3 electrons, and the charge configuration energies of the electrons are resonant. We set the local energy reference at this regime as $\mu_i(N) = 0$ eV for all dots, and refer to this condition as point N (see inset of Fig. 2a). Different features of the charge stability diagrams are also used to estimate the effective Hamiltonian parameters in our experimental system. The effective on-site interaction U_i is measured by extracting the local energy offset in dot i required to change the occupation from 1 electron to 2 electrons. The effective tunnel coupling term $t_{i,j}$ is measured by analyzing the width of the step in the charge sensing signal as the detuning between dots i and j is swept to transfer a single electron between them. Virtual gates provide knobs to effectively control the μ_i and $t_{i,j}$ parameters in the experimental system, by canceling the effects of cross-talk between gates. A more detailed description of the fabrication, operation, measurement protocols and implementation of the virtual gates can be found in the supplementary material and in Ref. [23].

The simple model described by Eqs. 1 and 2 already provides some useful insight into the parameter regimes that are relevant to the experiment. The ferromagnetic state is the ground state at large U/t, with a transition to a low-spin ground state occurring at $U/t = 18.7$. The quantum dot array used in this work has an average $U \approx 2.9$ meV across the four sites, with tunable nearest-neighbor tunnel couplings in the range of $0 < t \lesssim 20$ μeV. Unless otherwise stated, the couplings in these measurements are tuned to $t_{i,i+1} \approx 16$ μeV. This means that we are probing the regime where the ground state is expected to be ferromagnetic and the transition to the low-spin state is out of experimental reach (see Fig. 1b). Moreover, the expected energy gap between the ferromagnetic and low-spin states in the system is $E_{1/2} - E_{3/2} \approx 4$ μeV, which is comparable to the measured electron temperature $k_B T_e \approx 6$ μeV (70 mK) [23]. This complicates the measurement, because we cannot distinguish the ground state of the system at equilibrium. Instead, we need to drive the system out of equilibrium in order to try to amplify the probability in the ground state. To this end, we have developed techniques to probe the different energy levels and probe the spin state of the system on timescales faster than the thermal relaxation.

Measurement protocol

Since the sensing dots are only sensitive to charge tunneling events, a spin-to-charge conversion protocol is needed in order to perform measurements of the spin state of the system. We do this at point M, where $\mu_i^M \approx [-2.5, 0.0, 1.0, -0.5]$ meV (see inset of Fig. 2a). There, the ground charge state is $[2,0,0,1]$ (where $[n_1,n_2,n_3,n_4]$ corresponds to the number of electrons with dot number in the subscript), while the first excited charge state is $[1,1,0,1]$. These states have an uncoupled spin in dot 4, with the remaining 2 spins in a singlet $|S\rangle$ (triplet $|T\rangle$) configuration for the ground (first excited) state. The charge stability diagram in Fig. 2a is simulated and measured (inset) using a gate combination that allows to see both points N and M in the same diagram.

Fig. 2b shows the lowest three multiplets of the energy spectrum of the 3-electron system, along the line that connects point M to point N. Close to point M we see a typical double quantum dot spectrum corresponding to the $[2,0,0,1] \leftrightarrow [1,1,0,1]$ charge transition with the $|S\rangle$ and $|T\rangle$ branches, while in the region around point N the spins delocalize and we see branches corresponding to the quadruplets and doublets of the 3-electron system.

With this device, we can probe the spin state of the 3-electron system using the following protocol: 1 - repeatedly (10000 times) pulse rapidly from point N to point M, 2 - for each repetition, perform single-shot $|S\rangle/|T\rangle$ measurements using dots 1 and 2 and taking 2 out of the 3 electrons, and 3 - extract the triplet probability P_T. Under ideal conditions, this constitutes a 2-spin projective measurement of the 3-electron system, resulting in $P_T^{(3/2)} = 1$ when the 3-electron system is in a ferromagnetic state (any of the $s = 3/2$ quadruplets). In the low-spin sector ($s = 1/2$), there are two sets of doublet states available, one of which projects 2 spins to $|S\rangle$, while the other projects to $|T\rangle$ [26]. In this system the doublets are effectively degenerate (see Fig. 2b), and their hybridization will result in $P_T^{(1/2)} = 0.5$.

Due to the low ratio of energy level splitting to temperature at point N, we cannot probe the ground state of the system by way of relaxation. Instead, we apply a gate pulse sequence that follows the detuning range shown in the energy spectrum plotted in Fig. 2b. Using the pulse sequence drawn in Fig. 2c, a 2-spin singlet state with a third, free spin sitting on dot 4, is initialized by waiting at point M for 500 μs. Next we apply simultaneous pulses to the P_i gates of different amplitudes, such that we effectively pulse along the 'detuning proportion' p_ϵ axis in Fig. 2b (see also the line along the charge stability diagram in Fig. 2a), defined such that $\mu_i(p_\epsilon) = (1-p_\epsilon)\mu_i^M$. We then wait a time τ_{wait} at $\mu_i(p_\epsilon)$, before finally pulsing back to point M to perform the measurement. Importantly, the level crossings seen in Fig. 2b are in fact avoided level crossings with spin-orbit and nuclear hyperfine mediated coupling between the spin states [26]. This avoided level crossing allows to probe the different states

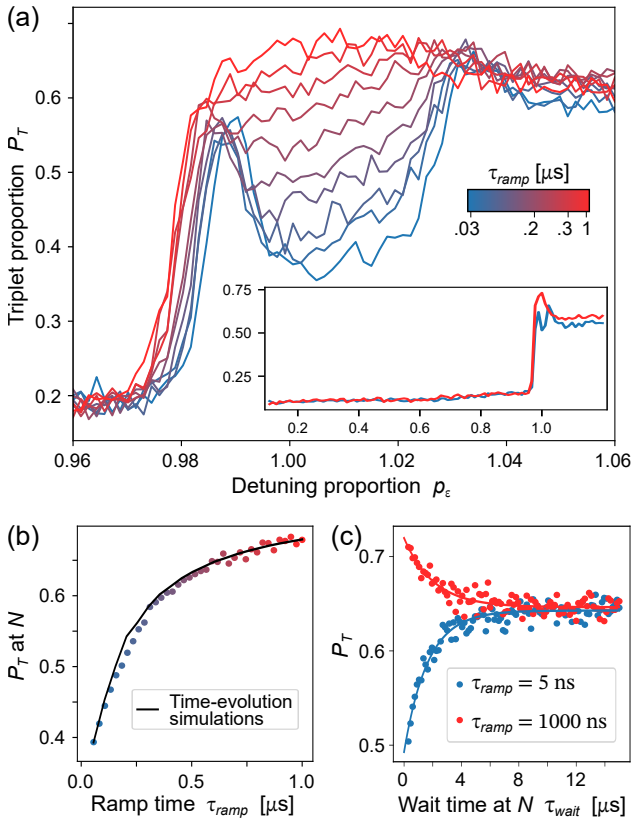

FIG. 3. (a) Measured P_T vs p_ϵ using the protocol described in the main text. Different curves correspond to different values of τ_{ramp}. The main figure focuses on the region close to point N, while the inset is zoomed out to the entire detuning range, for the 2 extreme values of τ_{ramp}. τ_{wait} is fixed to 50 ns (500 ns) for the main figure (inset). (b) Average P_T in the detuning region $1.00 < p_\epsilon < 1.01$ for a set of 40 measurements within the same τ_{ramp} range shown in (a). Black line is a fit made via time evolution simulations in which we initialize a statistical mixture of the two lowest energy eigenstates at $p_\epsilon = 0.8$ and sweep the potentials to $p_\epsilon = 1$ at different rates. The fit has the hyperfine coupling parameter δ_N as a free fitting parameter, and the extracted P_T curve from the model is scaled and offset to match the data at the minimum and maximum value of τ_{ramp}, to account for measurement imperfections [26]. (c) Thermal relaxation measurements. P_T is measured for increasing wait times at point N, for diabatic (dark) and adiabatic (light) passages. Solid lines are exponential fits as guide to the eye.

in the region around $p_\epsilon = 1$, by varying the ramp rate in the pulse sequence: a slow (fast) ramp rate results in an adiabatic (diabatic) passage through the avoided level crossings, so the ground (excited) state is reached. In practice, in order to avoid leakage to excited states along the way, 80% of the pulse is performed adiabatically, with the variable ramp time τ_{ramp} only for the remaining 20%. Varying τ_{wait} allows to study the relaxation dynamics in the system. As long as τ_{wait} is shorter than the thermal relaxation time-scale, the measurement of P_T will be able to distinguish between ferromagnetic

and low-spin states at point N.

MEASUREMENT RESULTS

Fig. 3a shows plots of $P_T(p_\epsilon)$ when we apply the experimental protocol described above. The inset of the figure shows the entire range of p_ϵ, highlighting that P_T remains at a low value for most of the range, with a sharp increase as p_ϵ approaches 1 (point N). This is consistent with expectation based on the energy spectrum plotted in Fig. 2b, where the initialized singlet state is not subject to any energy-level crossing until the region close to point N, where the levels cross and the electrons become delocalized in the array, leading to a sharp increase in the observed P_T. The non-zero triplet fraction at low values of p_ϵ is attributed partly to infrequent thermal excitations during the initialization stage–as a consequence of the finite electron temperature–and partly to a small probability of leakage to excited states during the pulse.

The main figure shows the measurement around point N, for a range of τ_{ramp}. In the region where $0.99 < p_\epsilon < 1.03$, a clear increase of P_T is observed as τ_{ramp} is increased, consistent with a gradual transition from diabatically pulsing into the low-spin state, to adiabatically pulsing into the ferromagnetic state, where P_T is maximum. For the faster pulses, we see 'peaks' of P_T at $p_\epsilon = 0.99$ and 1.03, where the pulse reaches the energy-level crossings, as all the spin states can be expected to quickly (i.e., much faster than the experimental timescales) mix by the nuclear hyperfine fields and spin-orbit coupling [27–29].

From the τ_{ramp} timescale for the diabatic to adiabatic transition (see Fig. 3b) we can extract information about the spin-coupling mechanisms at the avoided crossings. To this end we have expanded the model in Eq. 1, to include the effects of spin-orbit interaction and the hyperfine induced magnetic field gradients [26]. The model suggests that the random hyperfine field gradients dominate the spin coupling present at the avoided level crossing (i.e., around $p_\epsilon \approx 0.97$). We can use the model to fit the data in Fig. 3b, through time-evolution simulations [26], from which we estimate a hyperfine coupling parameter $\delta_N = 73 \pm 3$ neV, defined as the standard deviation of the Gaussian probability distribution of the hyperfine field in each dot [26]. The extracted δ_N is in agreement with previous observations and calculations, which have estimated 70 neV to 120 neV in similar GaAs quantum dot systems [29–31]. We note that the observed behavior can be qualitatively captured by a simple two-level Landau-Zener model [26].

If we keep $p_\epsilon = 1$ fixed and vary the wait time τ_{wait} spent at point N, we observe relaxation of the $s = 1/2$ and $s = 3/2$ states, reflected in the decay of P_T to an intermediate level between the P_T observed for slow and rapid sweeps, at the shortest τ_{wait} (see Fig. 3c). This is consistent with thermal equilibration in the system, in which the electron temperature is comparable to the

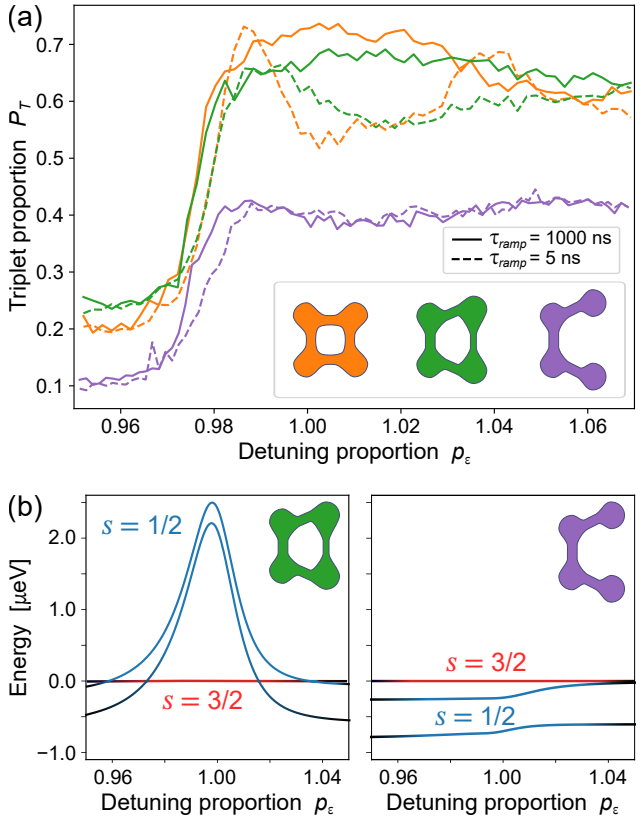

FIG. 4. (a) Comparison of 3 measurements with the following values of tunnel couplings $[t_{12}, t_{23}, t_{34}, t_{41}]$ (in μeV): [18.6, 15.3, 17.4, 18.6](orange); [15.7, 7.9, 20.3, 19.0](green); [18.2, 0.0, 21.1, 20.7](purple). The offsets between the curves are not attributed to the topology, but are due to small measurement-to-measurement variations in the thermal excitation rate during the initialization stage of the protocol. (b) Calculated energy spectrum as a function of detuning proportion, using the tunnel coupling values corresponding to the green (left) and purple (right) plots from (a).

energy gap between the $s = 1/2$ and $s = 3/2$ states at point N. The thermal equilibration occurs on a timescale $\tau_{relax} \sim 2$ μs. We note that we cannot directly assign the values of P_T to $s = 1/2$ and $s = 3/2$ populations, because the observed P_T is subject to measurement imperfections caused by mechanisms that are difficult to disentangle, such as the finite measurement bandwidth, the signal to noise ratio and $|T\rangle$ to $|S\rangle$ relaxation, as well as unwanted leakage to other states during the pulsed passages.

Boundary conditions and the Lieb-Mattis theorem

Considering that the square plaquette can be thought of as a 1D ring, the observation of a ferromagnetic ground state may appear to be in contradiction with the *Lieb-Mattis theorem* [25] which states that the ground state of a 1D array of electrons has the lowest possible spin. However, as later pointed out by Mattis himself [10] the Lieb-

Mattis theorem was only proven for 1D chains with open boundary conditions, explicitly excluding arrays with periodic boundary conditions such as the case of the plaquette. We can intuitively understand the difference between these two configurations when we consider how the hole tunnels to its next-nearest neighbor [32]. In a 2D plaquette, the hole has 2 possible paths to the next-nearest neighbor. If the system is initialized in any of the $s = 1/2$ configurations, the 2 paths will leave the system in 2 different configurations. On the other hand, for an $s = 3/2$ system the 2 paths are identical, and interfere constructively to lower the kinetic energy of the system. In contrast, in an open boundary 1D array, the kinetic energy of the hole is independent of the spin configurations of the neighboring electrons (i.e., there is only one path for the hole to follow through the array), therefore the total energy of the system will obey the Lieb-Mattis theorem.

One powerful feature of the quantum dot system is that the tunnel barriers can be tuned independently, allowing us to test different array topologies. In Fig. 4 we compare diabatic and adiabatic sweeps, as we raise the tunnel barrier that controls t_{23}, effectively transforming the plaquette into a system that behaves more like the 1D system described by Mattis. In the latter regime, we see that P_T becomes insensitive to sweep rate. Additionally, we no longer observe the peaks of P_T for the fast sweep rate, which we had associated with mixing at the avoided level crossings. From these observations we infer that for the open chain, the instantaneous ground state does not exhibit an avoided crossing between an $s = 1/2$ state and an $s = 3/2$ state as the system is taken to point N. This interpretation is also consistent with the numerical simulations of the energy spectrum shown in Fig. 4b.

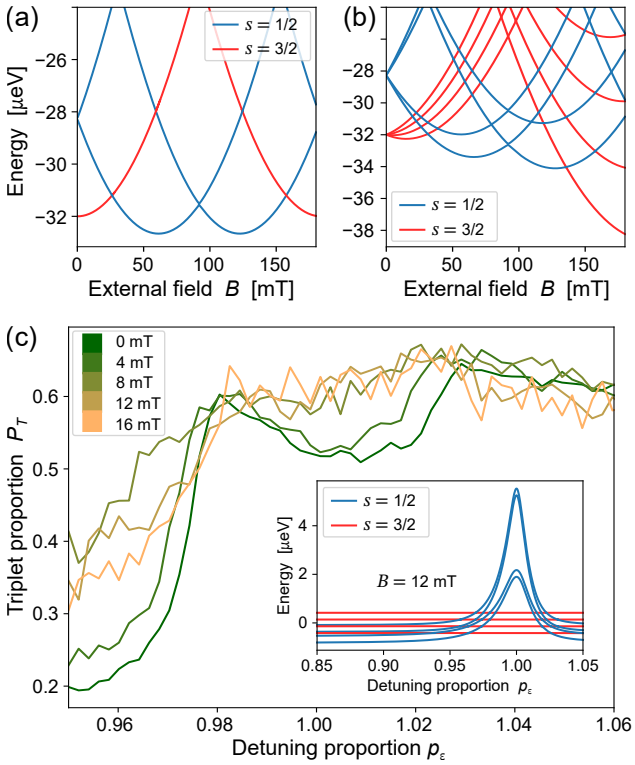

FIG. 5. **Applying an external magnetic field.** (a) Lowest eigenenergies of the $s = 1/2$ (blue) and $s = 3/2$ (red) states at point N as a function of magnetic field, obtained from the numerical model after including the effect of an Aharonov-Bohm phase (details in main text). (b) Same as (a) but with the addition of the Zeeman effect, and the lowest 4 eigenenergies of each s states are shown. (c) Experimental measurement using diabatic passage, for different fields in the range of 0 to 16 mT. Inset shows a numerically calculated spectrum at 12 mT, with the Aharonov-Bohm phase and Zeeman effect included in the model.

Destroying ferromagnetism with magnetic fields

Given that Nagaoka ferromagnetism can be explained through interference effects due to the trajectories of the hole around the ring, it then follows that a magnetic flux through the plaquette will add an Aharonov-Bohm phase [33] that disturbs the interference effects. We capture this effect in the theoretical model by modifying the second term in Eq. 1 as [26]: $-\sum_{\langle j,k\rangle\sigma} t_{j,k} \exp(-i\varphi_{jk})\, c^\dagger_{j\sigma} c_{k\sigma}$. We use the gauge in which $\varphi_{41} = \frac{2\pi\Phi}{\Phi_0}$, where $\Phi = B\ell^2$ is the flux generated by a magnetic field B through the plaquette with estimated distance between nearest-neighbor dots ℓ, and $\Phi_0 = h/e$ is the flux quantum. Using this gauge, the phases for the other links vanish. In addition, the application of an external field subjects the system to the Zeeman effect, causing a spin-dependent energy offset $E_Z = g\mu_B Bm$ to each eigenstate, where $g = -0.4$ is the electron g-factor in GaAs and μ_B is the Bohr magneton.

Fig. 5a shows the effect of the magnetic flux on the spectrum, ignoring the Zeeman effect. The lowest $s = 1/2$ and $s = 3/2$ levels at point N are shown as a function of the applied field, where periodic crossings can be observed. In the range $30 < B < 160$ mT, the system ground state transitions to the low-spin state, with the–perhaps counterintuitive–implication that we can destroy the ferromagnetic state by applying a magnetic field. Additionally, this effect highlights that the ferromagnetic state in this system is dominated by the Nagaoka effect and not by long-range interactions. Indeed, the ab initio calculations suggest that long-range interactions only account for $\sim 20\%$ of the ferromagnetic polarization. When we include the Zeeman effect (see Fig. 5b) the picture becomes more complicated, because both Zeeman and orbital effects cause perturbations of similar energy scales.

From this initial numerical analysis it is clear that the experimental characterization of the applied external field will be challenging, due to the increased complexity of the spectral structure of the spin states as a function of field. The small energy splittings that appear both at point N, as well as at lower p_ϵ values (see inset of

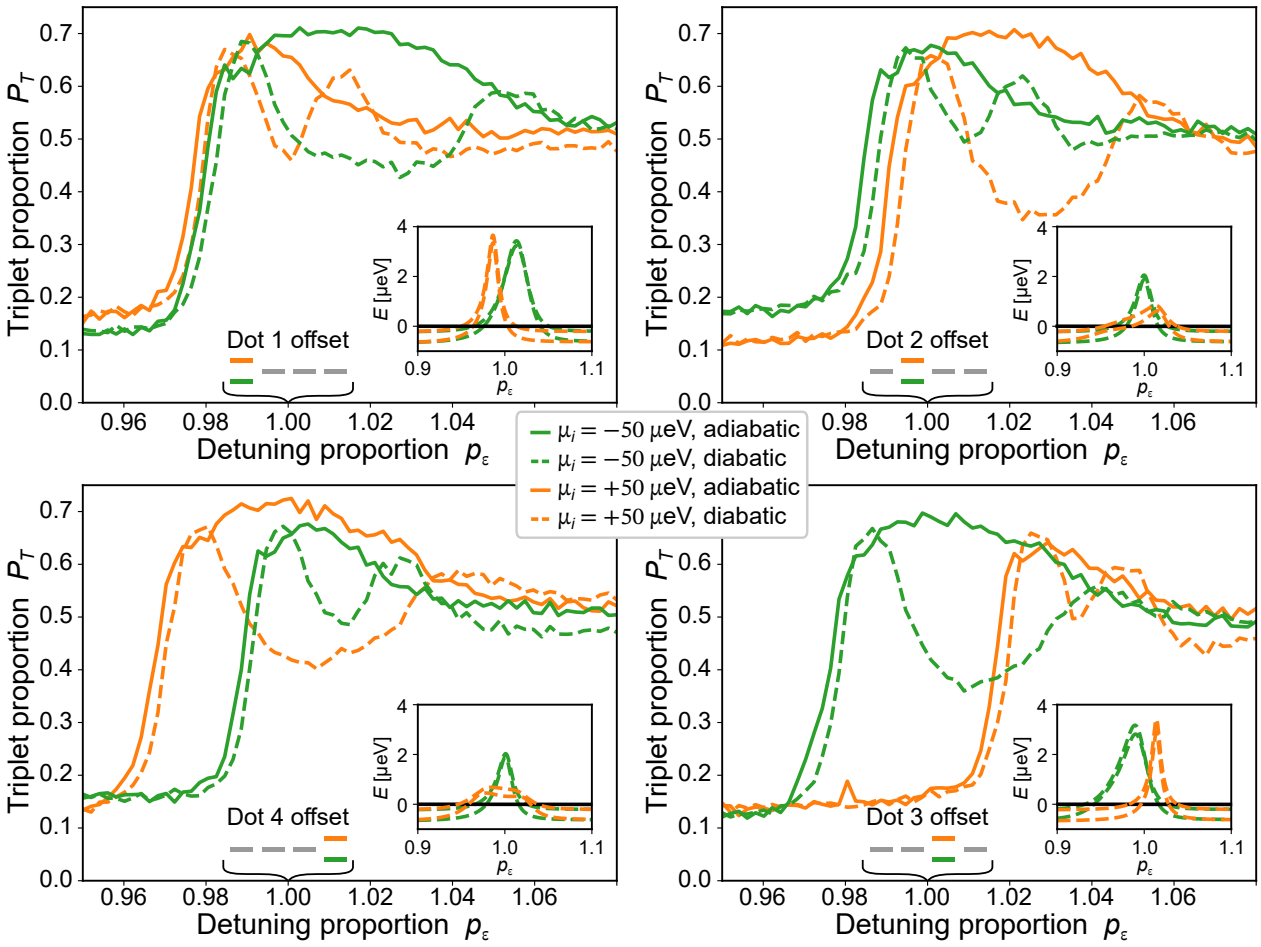

FIG. 6. Experimental measurements with point N purposefully redefined to have a ± 50 μeV offset on each of the 4 dots. Panels correspond to offsets in dots 1 to 4, clockwise from the top-left. Insets show numerically calculated spectra for the same experimental condition.

Fig. 5c) are expected to cause mixing of the spin states during the adiabatic pulses. To minimize this mixing, we adjusted the pulsing protocol such that we pulse adiabatically (1 μs ramp) to $p_\epsilon = 0.2$, then pulse diabatically (5 ns ramp) the rest of the way. The results in Fig. 5c show that from 4 to 8 mT P_T increases at point N, and we stop observing the characteristic dip. Note that the range of field that we were able to probe is still below the estimated ground state transition point (~ 30 mT). Therefore, we infer that the observed increase in P_T is the effect of hybridization of the $s = 1/2$ and $s = 3/2$ states as their energy gap reduces. We cannot claim that the observed hybridization of states is occurring solely at point N, as it is evident from the increase in P_T at $p_\epsilon < 0.97$ (i.e. prior to the energy-level crossings) that some of the mixing is occurring during the pulse. However, we do see that P_T in all plots converge at the energy-level crossings ($p_\epsilon \approx 0.97$ and $p_\epsilon \approx 1.03$) suggesting that the Aharonov-Bohm orbital effects are partly responsible for the additional mixing in the region around point N.

Sensitivity to local energy offsets

We also use the tunability available in quantum dot systems to study the effects of disorder of the local potential present in each dot. For the plots in Fig. 6, we modified the experimental protocol used to probe the states at point N, pulsing instead to a point N', where the local energy of one of the dots is offset by ± 50 μeV. We can do this by employing the *virtual gates* technique [19, 23], which gives access to control knobs that map a linear combination of P_i gates onto local dot energy offsets. The insets of the panels in Fig. 6 show the expected energy spectra when we simulate the experimental conditions using the model in Eq. 1. The spectra show that for all cases there remains a region in the detuning trajectory where the ferromagnetic state is the ground state, but both the width and the position of this region around point N' varies with the different local offsets applied. The experimental results in the main panels show excellent qualitative agreement with the variations observed in the calculated spectra, further confirming the valid-

ity of the experimental protocol. Remarkably, we have also pushed the offset of dot 1 to the range −100 to +800 μeV and the system still shows signs of the ferromagnetic ground state (see Fig. S5).

DISCUSSION

In this work we have presented the first measurements showing experimental evidence of Nagaoka's 50-year old theory in a small scale system. The large degree of tunability, high ratio of interaction strength to temperature, and fast measurement techniques available to quantum dot systems, allowed observing both the ferromagnetic ground state and the low-spin excited state of an almost-half-filled lattice of electrons. Even though the problem of 3 electrons in a 4-site plaquette can be solved analytically using the Hubbard picture, a complete description of this experimental system that includes all its available orbitals is not easily tractable, analytically or numerically. Indeed, the computational cost of the ab initio calculation, with all interaction terms being considered, is on the order of 10000 CPU hours. In addition, this small scale quantum simulation provides value beyond proof-of-principle in two important ways. First, by performing a quantum simulation involving charge and spin states, it builds on previous demonstrations [19] that quantum dot systems can be useful simulators of the Hubbard model, despite their inhomogeneities in the potential shape and local energies. Additionally, small scale simulations on tractable models can be used to systematically benchmark the performance of devices as the scale-up technology develops towards devices that can perform classically intractable simulations. Finally, in this work we showed a flavor of the capabilities for studying the sensitivity to disorder, and these experiments already revealed some surprising effects, when we found that the Nagaoka condition can still be observed after offsetting a local energy by amounts much larger than the tunnel coupling. This can readily be studied in further detail, along with other possibilities for exploring the effects of disorder, which could bring insights into e.g., the stability of the ferromagnetic state.

This experiment is an important step forward in answering the question of whether itinerant magnetism can occur in real systems. Larger realizations of similar quantum dot systems (or any other experimentally controllable system), such as $2 \times N$ or $M \times N$ arrays can shed more light on the discussion. As the system becomes larger the exchange interaction grows proportionally to the system size, creating a competition against the hopping energy that is characteristic of Nagaoka ferromagnetism, and leaving the fate of the Nagaoka mechanism in larger systems in the realm of the unknown.

ACKNOWLEDGMENTS

We acknowledge useful input and discussions with M. Chan, S. Philips, Y. Nazarov, F. Liu, L. Janssen, T. Hensgens, T. Fujita and all of the Vandersypen team, as well as experimental support by L. Blom, C. van Diepen, P. Eendebak, R. Schouten, R. Vermeulen, R. van Ooijik, H. van der Does, M. Ammerlaan, J. Haanstra, S. Visser and R. Roeleveld. L.M.K.V. thanks the NSF-funded MIT-Harvard Center for Ultracold Atoms for its hospitality. **Funding:** J.P.D., U.M., L.M.K.V. acknowledge the Netherlands Organization for Scientific Research (FOM projectruimte and NWO Vici). V.P.M., L.M.K.V. the European Research Council (ERC-Synergy). Y.W. acknowledges the Postdoctoral Fellowship in Quantum Science of the Harvard-MPQ Center for Quantum Optics and AFOSR-MURI Quantum Phases of Matter (Grant No. FA9550-14-1-0035). C.R., W.W. acknowledge the Swiss National Science Foundation. M.S.R. acknowledges The Villum Foundation. **Author contributions:** B.W., M.S.R., E.D., L.M.K.V. had equal contribution in conceptualization; Experimental investigation and methodology was performed with equal contribution from J.P.D., U.M.; Theoretical investigation was led by J.P.D., V.P.M., B.W. (extended Hubbard models), and Y.W. (ab initio model); J.P.D. led the data curation and software, with support from U.M., V.P.M.; J.P.D., U.M. had equal contribution in the formal analysis, with support from V.P.M.; L.M.K.V. led the funding acquisition and supervision; U.M. led the resources (device fabrication) with support from J.P.D.; C.R., W.W. led the resources (heterostructure growth). J.P.D. led the writing - original draft, with review and editing support from U.M., V.P.M., Y.W., M.S.R., E.D., L.M.K.V. **Competing interests:** authors have no competing interests.

[1] A. Auerbach, *Interacting Electrons and Quantum Magnetism* (Springer New York, 1994).
[2] D. C. Mattis, *The Theory of Magnetism Made Simple* (World Scientific, 2006).
[3] E. C. Stoner, P. Roy. Soc. Lon. A **165**, 372 (1938).
[4] P. Fazekas, *Lecture notes on electron correlation and magnetism* (World Scientific, 1999).
[5] G.-B. Jo, Y.-R. Lee, J.-H. Choi, C. A. Christensen, T. H. Kim, J. H. Thywissen, D. E. Pritchard, and W. Ketterle, Science **325**, 1521 (2009).
[6] D. Pekker, M. Babadi, R. Sensarma, N. Zinner, L. Pollet, M. W. Zwierlein, and E. Demler, Phys. Rev. Lett. **106**, 050402 (2011).
[7] H. Tasaki, Progress of Theoretical Physics **99**, 489 (1998).
[8] Y. Nagaoka, Phys. Rev. **147**, 392 (1966).
[9] J. Hubbard, P. Roy. Soc. Lon. A **276**, 238 (1963).
[10] D. C. Mattis, Int. J. Nanosci. **02**, 165 (2003).
[11] E. Nielsen and R. N. Bhatt, Phys. Rev. B **76**, 161202(R)

(2007).
[12] A. Oguri, Y. Nisikawa, Y. Tanaka, and T. Numata, J. Magn. Magn. Mater. **310**, 1139 (2007).
[13] J. von Stecher, E. Demler, M. D. Lukin, and A. M. Rey, New J. Phys. **12**, 055009 (2010).
[14] I. Bloch, J. Dalibard, and S. Nascimbène, Nat. Phys. **8**, 267 (2012).
[15] L. P. Kouwenhoven, D. G. Austing, and S. Tarucha, Rep. Prog. Phys. **64**, 701 (2001).
[16] W. G. van der Wiel, S. D. Franceschi, J. M. Elzerman, T. Fujisawa, S. Tarucha, and L. P. Kouwenhoven, Rev. Mod. Phys. **75**, 1 (2002).
[17] R. Hanson, L. Kouwenhoven, J. Petta, S. Tarucha, and L. Vandersypen, Rev. Mod. Phys. **79**, 1217 (2007).
[18] P. Barthelemy and L. M. K. Vandersypen, Ann. Phys. (Leipzig) **525**, 808 (2013).
[19] T. Hensgens, T. Fujita, L. Janssen, X. Li, C. J. V. Diepen, C. Reichl, W. Wegscheider, S. D. Sarma, and L. M. K. Vandersypen, Nature **548**, 70 (2017), 1702.07511v1.
[20] R. Thalineau, S. Hermelin, A. D. Wieck, C. Bauerle, L. Saminadayar, and T. Meunier, Appl. Phys. Lett. **101**, 103102 (2012).
[21] M. Seo, H. K. Choi, S.-Y. Lee, N. Kim, Y. Chung, H.-S. Sim, V. Umansky, and D. Mahalu, Phys. Rev. Lett. **110** (2013), 10.1103/physrevlett.110.046803.
[22] A. Noiri, K. Kawasaki, T. Otsuka, T. Nakajima, J. Yoneda, S. Amaha, M. R. Delbecq, K. Takeda, G. Allison, A. Ludwig, A. D. Wieck, and S. Tarucha, Semicond. Sci. Technol. **32**, 084004 (2017).
[23] U. Mukhopadhyay, J. P. Dehollain, C. Reichl, W. Wegscheider, and L. M. K. Vandersypen, Appl. Phys. Lett. **112**, 183505 (2018).
[24] P.-A. Mortemousque, E. Chanrion, B. Jadot, H. Flentje, A. Ludwig, A. D. Wieck, M. Urdampilleta, C. Bauerle, and T. Meunier, http://arxiv.org/abs/1808.06180v1 (2018), http://arxiv.org/abs/1808.06180v1.
[25] E. Lieb and D. Mattis, Phys. Rev. **125**, 164 (1962).
[26] See supplementary text.
[27] A. V. Khaetskii, D. Loss, and L. Glazman, Phys. Rev. Lett. **88**, 186802 (2002).
[28] I. A. Merkulov, A. L. Efros, and M. Rosen, Phys. Rev. B **65**, 205309 (2002).
[29] E. A. Chekhovich, M. N. Makhonin, A. I. Tartakovskii, A. Yacoby, H. Bluhm, K. C. Nowack, and L. M. K. Vandersypen, Nat. Mater. **12**, 494 (2013).
[30] J. R. Petta, Science **309**, 2180 (2005).
[31] F. H. L. Koppens, Science **309**, 1346 (2005).
[32] D. C. Mattis, *The theory of magnetism I: statics and dynamics*, Springer series in solid-state sciences (Springer, 1981).
[33] Y. Aharonov and D. Bohm, Phys. Rev. **115**, 485 (1959).

Supplementary material for: Nagaoka ferromagnetism observed in a quantum dot plaquette

Juan P. Dehollain, Uditendu Mukhopadhyay, Vincent P. Michal, Yao Wang, Bernhard Wunsch, Christian Reichl, Werner Wegscheider, Mark S. Rudner, Eugene Demler, and Lieven M.K. Vandersypen

DEVICE FABRICATION AND METHODS

The experiment was performed using an array of four gate-defined quantum dots in a 2×2 geometry. We employed a double-layer gate-structure to form this dot array. The first layer of gates–which includes all gates except D_0–was created using electron-beam lithography, evaporation and lift-off of Ti/Au with 5/20 nm thickness (see Fig. 1a of the main text). We then fabricate a 1.5×0.2 nm dielectric slab on top of the gates C_3 and P_3, using electron-beam lithography, sputtering and lift-off of SiN_x slab with 50 nm thickness. Finally, the D_0 gate is created using the same process as the other gates, with 10/100 nm thick Ti/Au. This gate runs over the gate C_3 before contacting the substrate at the center of the dot array. The gates created in the first layer are 30 nm wide, whereas the width of the D_0 gate is 100 nm.

Different parameters of the dot array can be controlled using voltages on different gates. The P_i gates are designed to control the electron filling of dot i by adjusting the dot chemical potential μ_i. Gates D_0 and C_i are designed to control the tunnel coupling $t_{i,j}$, while gates B_i and C_{i+1} are designed to control the coupling between dot i and its reservoir. In reality, the proximity between the gates causes non-negligible cross capacitances, preventing independent control of the parameters that the gates were designed control. For some of the tuning stages, we make use of linear combination of gate voltages–known as *virtual gates* [19,23]–to provide a direct experimental knob to the parameter of interest. We use charge stability diagrams [16] to identify the charge state of the system as a function of different P_i voltages. These diagrams are also used to measure and tune the effective $t_{i,j}$ parameters independently, using the technique described in detail in Refs. [19,23], which requires analyzing the interdot transition of a single electron across dots i and j.

In order to observe signatures of Nagaoka ferromagnetism, we need to tune the system such that it is loaded with three electrons isolated from the reservoirs and these three electrons must be itinerant in the four dot system. In Fig. S1, we show some sample charge stability diagrams and describe the tuning method used to tune the gate voltages to identify point N. To tune $t_{i,i+1}$ close to point N, we first localize 2 of the electrons in dots $i+2$, $i+3$ (i.e. by slightly lowering μ_{i+2}, μ_{i+3}), and keep dots i, $i+1$ resonant using the remaining electron to measure their tunnel coupling. Here we use cyclic dot indices with $i = \{1, 2, 3, 4\}$.

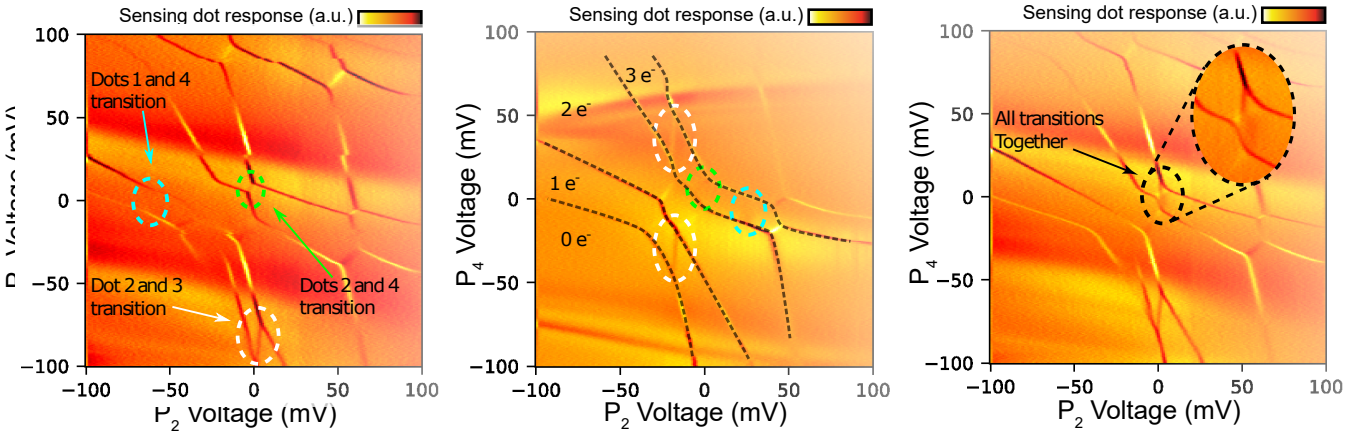

FIG. S1. Sample stability diagrams showing how we tune to the Nagaoka condition. We have highlighted the visible interdot transitions (identified in the right panel), where the electrochemical potentials of two dots become resonant (i.e., an electron is allowed tunnel between the two dots). In the center panel, dashed black lines delimit the regions with a fixed total electron occupation in the system. From the left to right panels, we gradually tune the gate voltages in order to reach the Nagaoka condition, where the three visible interdot transitions are aligned in the three-electron configuration (right panel). The intersite interaction in the system provides an effective isolation from the reservoirs for a narrow range of gate voltages, such that the system can remain stable with three electrons in the resonant configuration.

Next, we identify the gate voltages suitable to perform the two spin projection measurement (point M in Fig. 2a in the main text). Once we have identified point M and fine-tuned the gates to optimize the spin-readout fidelity, we define a linear combination of P_i voltages that joins the points M and N by a straight line in gate voltage space. This virtual gate enables us to probe the system along the 'detuning proportion' p_ϵ axis in Fig. 2b in the main text.

EXTENDED FERMI-HUBBARD MODELS USED TO SIMULATE DIFFERENT EXPERIMENTS IN THE MAIN TEXT

In this section we will describe the different parameters that are included in the model Hamiltonians that we refer to in the main text for analytical and numerical simulations. We begin with the simplest Fermi-Hubbard model of a 2×2 site plaquette with 3 electrons, and add from there different parameters as we increase the complexity of the model. The simplest Hamiltonian we describe ($\mathcal{H}_0$) has been solved analytically with the aid of *Mathematica*. The more complex Hamiltonians in the following subsections were solved numerically, using mainly the eigensolvers from the *Python*-based *Scipy* package, with the exception of the time-evolution simulations, which were solved using an in-house solver package [S1].

Representation of the quantum states

We represent the quantum states on the 2×2 plaquette as

$$|\psi\rangle = \sum_{\{n_{i\sigma}\}} a(\{n_{i\sigma}\})|\{n_{i\sigma}\}\rangle. \tag{S1}$$

The basis consists of the states specified by the occupations of the electrons on the lattice and their spin projections:

$$|\{n_{i\sigma}\}\rangle = |n_{1\uparrow}n_{2\uparrow}n_{3\uparrow}n_{4\uparrow}n_{1\downarrow}n_{2\downarrow}n_{3\downarrow}n_{4\downarrow}\rangle, \tag{S2}$$

with $n_{i\sigma} = 0$ or 1. For N electrons on the plaquette we have $\sum_{i\sigma} n_{i\sigma} = N$ and the basis states consist of all combinations of the occupations at fixed N. Hence $N = 3$ corresponds to a space of the quantum states of dimension $8!/5!3! = 56$.

The on-site energy and the Coulomb repulsion terms of the Hamiltonian $\sum_i U_i n_{i\uparrow}n_{i\downarrow} - \sum_i \mu_i n_i$ are diagonal in this basis. Tunneling involves the off-diagonal matrix elements [S2]:

$$\langle \dots 1_{i\sigma} \dots 0_{j\sigma'} \dots | c^\dagger_{i\sigma} c_{j\sigma'} | \dots 0_{i\sigma} \dots 1_{j\sigma'} \dots \rangle = (-1)^{\sum_{\ell=i\sigma+1}^{j\sigma'-1} n_\ell}, \tag{S3}$$

where ℓ goes over the elements between $i\sigma$ and $j\sigma'$ (exclusive) in the list (S2). The Hamiltonian commutes with the spin operators $\mathbf{S}^2$ and S_z and its eigenstates are also spin eigenstates $|s, m\rangle_\alpha$:

$$\mathbf{S}^2|s,m\rangle_\alpha = s(s+1)|s,m\rangle_\alpha \quad \text{and} \quad S_z|s,m\rangle_\alpha = m|s,m\rangle_\alpha,\ m = -s, -s+1, \dots, s. \tag{S4}$$

The spin operators are $\mathbf{S}^2 = S_z^2 + \frac{1}{2}(S_+S_- + S_-S_+)$, $S_z = \frac{1}{2}\sum_i (n_{i\uparrow} - n_{i\downarrow})$, $S_+ = \sum_i c^\dagger_{i\uparrow} c_{i\downarrow}$, and $S_- = \sum_i c^\dagger_{i\downarrow} c_{i\uparrow}$. The label α distinguishes between the states with the same quantum numbers s and m. For three electrons in the absence of a magnetic field those states consist of energy degenerate $s = 3/2$ quadruplets and two sets of energy degenerate $s = 1/2$ doublets. In the low-energy sector relevant to the study, α distinguishes between the two sets of $s = 1/2$ doublets.

Basic construction of the 3-electron filled plaquette Fermi-Hubbard Hamiltonian

In the simplest version of the model, the system is constrained to having 3 electrons and each dot can be occupied with at most 2 electrons, subject to Pauli exclusion (i.e. double occupation of a dot must be of opposite spin). For this section, the on-site interaction U and tunnel coupling t are taken to be equal for all sites. For now we do not consider any spin coupling or spin-dependent splitting, therefore the Hamiltonian can be divided into two independent blocks, one for the $m = \pm 3/2$ states (parallel spins) and another for the $m = \pm 1/2$ states (one flipped spin):

$$\boldsymbol{\mathcal{H}_0 = \mathcal{H}_{3/2} + \mathcal{H}_{1/2}} \tag{S5}$$

and for each block it is sufficient to solve for one of the m projections and assume another degenerate set of states for the opposite m projection. As will be shown, these assumptions reduce the dimensions of the Hamiltonians to 4 for $\boldsymbol{\mathcal{H}_{3/2}}$ and 24 for $\boldsymbol{\mathcal{H}_{1/2}}$, making them simpler to solve analytically.

The quantum states for $\boldsymbol{\mathcal{H}_{3/2}}$ will be

$$|\psi_{3/2}\rangle = a_1|0\uparrow\uparrow\uparrow\rangle + a_2|\uparrow 0\uparrow\uparrow\rangle + a_3|\uparrow\uparrow 0\uparrow\rangle + a_4|\uparrow\uparrow\uparrow 0\rangle \tag{S6}$$

with the Hamiltonian

$$\boldsymbol{\mathcal{H}_{3/2}} = \begin{bmatrix} 0 & -t & 0 & -t \\ -t & 0 & -t & 0 \\ 0 & -t & 0 & -t \\ -t & 0 & -t & 0 \end{bmatrix} \tag{S7}$$

with eigenvalues $\{-2t, 0, 2t\}$.

For the block with $m = \pm 1/2$, double occupation is allowed, therefore we need to consider more available states. We construct the Hamiltonian by first fixing the flipped spin in one dot and working out all the possible states in the basis. For example, a down spin in dot 1 results in the basis sub-set

$$|\psi'_{1/2}\rangle = a_1|2\uparrow 00\rangle + a_2|20\uparrow 0\rangle + a_3|200\uparrow\rangle + a_4|\downarrow 0\uparrow\uparrow\rangle + a_5|\downarrow\uparrow 0\uparrow\rangle + a_6|\downarrow\uparrow\uparrow 0\rangle \tag{S8}$$

from which we then construct

$$\boldsymbol{\mathcal{H}'_{1/2}} = \begin{bmatrix} U & -t & 0 & 0 & t & 0 \\ -t & U & -t & -t & 0 & t \\ 0 & -t & U & 0 & -t & 0 \\ 0 & -t & 0 & 0 & -t & 0 \\ t & 0 & -t & -t & 0 & -t \\ 0 & t & 0 & 0 & -t & 0 \end{bmatrix} \tag{S9}$$

The same matrix can be used for the subspace with the flipped spin on each of the other dots. To finish constructing the 24-dimensional Hamiltonian, we need to then work out the hopping matrices for the spin down, which results in the full Hamiltonian:

$$\boldsymbol{\mathcal{H}_{1/2}} = \begin{bmatrix} \boldsymbol{\mathcal{H}'_{1/2}} & \boldsymbol{T} & 0 & \boldsymbol{T}^\intercal \\ \boldsymbol{T}^\intercal & \boldsymbol{\mathcal{H}'_{1/2}} & \boldsymbol{T} & 0 \\ 0 & \boldsymbol{T}^\intercal & \boldsymbol{\mathcal{H}'_{1/2}} & \boldsymbol{T} \\ \boldsymbol{T} & 0 & \boldsymbol{T}^\intercal & \boldsymbol{\mathcal{H}'_{1/2}} \end{bmatrix} \quad \text{where} \quad \boldsymbol{T} = \begin{bmatrix} 0 & 0 & t & 0 & 0 & 0 \\ 0 & 0 & 0 & 0 & t & 0 \\ 0 & 0 & 0 & 0 & 0 & t \\ -t & 0 & 0 & 0 & 0 & 0 \\ 0 & -t & 0 & 0 & 0 & 0 \\ 0 & 0 & 0 & -t & 0 & 0 \end{bmatrix} \tag{S10}$$

The lowest two eigenvalues of this Hamiltonian are $-2t$ (two states) and $-\sqrt{3}t - \frac{5t^2}{U}$ (four states). The former correspond to the $m = \pm 1/2$ states of the quadruplets with total spin $s = 3/2$. The remaining four states correspond to the two $s = 1/2$ doublets (with $m = \pm 1/2$).

As expected for a 3-spin system, the 8 lowest eigenenergies of this Hamiltonian contain 4 degenerate ferromagnetic quadruplets and the 2 sets of degenerate low-spin doublets.

Site specific parameters and local energy offsets

The first increase in the level of complexity for the model is to make the parameters site specific (U_i and $t_{i,j}$), as well as to add site specific local energy offsets μ_i. The resulting Hamiltonian

$$\boldsymbol{\mathcal{H}_1} = -\sum_{\langle i,j\rangle\sigma} t_{i,j} c^\dagger_{i\sigma} c_{j\sigma} + \sum_i U_i n_{i\uparrow} n_{i\downarrow} - \sum_i \mu_i n_i \tag{S11}$$

can be constructed in similar way as described above, with the addition of the corresponding diagonal μ_i elements. We numerically solve this Hamiltonian to obtain the p_ϵ dependent energy spectra shown in the main manuscript.

Spin coupling terms

In order to capture the τ_{ramp} dependence of our experiments, we have added to the model the effects of spin-orbit coupling and hyperfine interactions, the two most important mechanisms that lead to spin flipping in GaAs [S3]. Since we are now considering spin coupling, we need the full quantum state representation with the 56-dimensional Hamiltonian.

For the quantum dot plaquette we have computed the matrix elements of the spin-orbit coupling Hamiltonian that accounts for the Bychkov-Rashba and the Dresselhaus effects for GaAs grown in the the crystallographic direction [001]:

$$\mathcal{H}_{so} = \alpha(p_x\sigma_y - p_y\sigma_x) + \beta(-p_x\sigma_x + p_y\sigma_y). \tag{S12}$$

here $\alpha = e\gamma_b\langle\mathcal{E}\rangle/\hbar$ and $\beta = \gamma_d\langle k_z^2\rangle/\hbar$ where $e > 0$ is the elementary charge, and $\mathcal{E}$ is the electric field at the interface of the structure. For GaAs $\gamma_b \approx 5.2 \times 10^{-2}\,\mathrm{nm}^2$ and $\gamma_d \approx 27.6\,\mathrm{meV.nm}^3$ [S4]. The axes of the coordinate system x and y correspond to the directions [100] and [010]. When spin-orbit coupling is weak we may take as a basis the Wannier states $|j\rangle$ that are localized on the dots indexed by j. In this basis the matrix elements of Eq. S12 are

$$\langle j|\mathcal{H}_{so}|k\rangle = \alpha(p_x^{jk}\sigma_y - p_y^{jk}\sigma_x) + \beta(-p_x^{jk}\sigma_x + p_y^{jk}\sigma_y), \tag{S13}$$

where $p_a^{jk} = \langle j|p_a|k\rangle$, $a = x, y$. Those matrix elements vanish if $j = k$. Then in the second quantized form Eq. S12 reads

$$\mathcal{H}_{so} = \sum_{jk\sigma\sigma'} c_{j\sigma}^\dagger \omega^{jk}\cdot\sigma^{\sigma\sigma'} c_{k\sigma'}, \tag{S14}$$

with $\omega^{jk}\cdot\sigma^{\sigma\sigma'} = (-\alpha p_y^{jk} - \beta p_x^{jk})\sigma_x^{\sigma\sigma'} + (\alpha p_x^{jk} + \beta p_y^{jk})\sigma_y^{\sigma\sigma'}$. The unit vector in the direction of the dots j and k is $\hat{\ell}_{jk} = \cos(\theta_{jk})\hat{x} + \sin(\theta_{jk})\hat{y}$. Eliminating the matrix elements of the momentum in the direction perpendicular to $\hat{\ell}_{jk}$, Eq. S14 becomes

$$\mathcal{H}_{so} = \sum_{jk\sigma\sigma'} c_{j\sigma}^\dagger p_\ell^{jk}\big((-\alpha\sin(\theta_{jk}) - \beta\cos(\theta_{jk}))\sigma_x^{\sigma\sigma'} + (\alpha\cos(\theta_{jk}) + \beta\sin(\theta_{jk}))\sigma_y^{\sigma\sigma'}\big)c_{k\sigma'}. \tag{S15}$$

Here $p_\ell^{jk} = m\langle j|\dot{\ell}|k\rangle = imt_{jk}\ell_{jk}/\hbar$, where m is the effective mass of the electron, $\ell_{jk} = \ell_j - \ell_k$ with ℓ_j the coordinate of dot j on the (jk) axis, and t_{jk} equals minus the matrix element of the one-electron Hamiltonian. Therefore

$$\mathcal{H}_{so} = \sum_{\langle j,k\rangle} t_{jk}c_{j\uparrow}^\dagger\big(\frac{\ell_{jk}}{\lambda_b}e^{-i\theta_{jk}} - i\frac{\ell_{jk}}{\lambda_d}e^{i\theta_{jk}}\big)c_{k\downarrow} + h.c., \tag{S16}$$

where jk are restricted to neighboring dots and we define the length scales $\lambda_b = \hbar/m\alpha$ and $\lambda_d = \hbar/m\beta$. Typically $\langle k_z^2\rangle \sim 0.02\,\mathrm{nm}^{-2}$ and $\langle e\mathcal{E}\rangle \sim 3\,\mathrm{meV/nm}$. So $\lambda_b \approx 7\,\mu$m and $\lambda_d \approx 2\,\mu$m, for neighbor quantum dots ($\ell_{jk} \approx 0.15\mu$m), giving $\ell_{jk}/\lambda_b \sim 0.02$ and $\ell_{jk}/\lambda_d \sim 0.08$.

The large abundance of nuclear spins in the GaAs crystal means that each site in the plaquette will be hyperfine coupled to a number of randomly oriented nuclear spins, causing each site to experience a slightly different Overhauser field. This interaction is described by the hyperfine coupling Hamiltonian [17,27,28]:

$$\mathcal{H}_{hf} = \mathbf{S}\cdot\mathbf{h}_N. \tag{S17}$$

Here $\mathbf{S} = (\sigma_x, \sigma_y, \sigma_z)/2$ is the electron spin operator, $\mathbf{h}_N = \sum_i A_i\mathbf{I}_i$, $A_i = Av_0|\psi(\mathbf{r}_i)|^2$ is the coupling parameter with nucleus i having spin operator $\mathbf{I}_i$, $\psi(\mathbf{r}_i)$ is the electron envelope wave function at the nuclear site $\mathbf{r}_i$, and v_0 is the volume of the crystal cell. Hence $\mathbf{B}_N = \mathbf{h}_N/g\mu_B$ is the nuclear magnetic field acting on the electron with g-factor g, and μ_B is the Bohr magneton.

The classical probability distribution of h_{Na} ($a = x, y$ or z) is normal [27,28]: $P(h_{Na}) = \frac{1}{\sqrt{2\pi\delta_N^2}}\exp(-h_{Na}^2/2\delta_N^2)$. The typical magnitude of the field component is $\delta_N \sim A/\sqrt{N} \ll h_{N\max} \sim A$, with N the number of nuclei covered by the envelope function of the electron and $h_{N\max}$ the magnitude of the field when the nuclear spins are fully polarized. For GaAs: $N \sim 10^6$ and $B_{N\max}/\sqrt{N}$ is of the order of a few mT [17], hence $h_{N\max}/\sqrt{N} \sim 0.1\,\mu$eV.

Since our basis states are eigenstates of the Pauli matrix σ_z, we express Eq. S17 as:

$$\mathcal{H}_{hf} = \frac{1}{2}\left(\sigma_z h_{Nz} + \sigma_+\left(h_{Nx} - ih_{Ny}\right) + \sigma_-\left(h_{Nx} + ih_{Ny}\right)\right), \tag{S18}$$

where $\sigma_\pm = (\sigma_x \pm i\sigma_y)/2$. We numerically implement Eq. S18 and the nuclear fields of the four quantum dots are taken to be independent. In Fig. S2a-c we show that the effect of the hyperfine coupling dominates over spin-orbit coupling, in the detuning region of the energy level crossings.

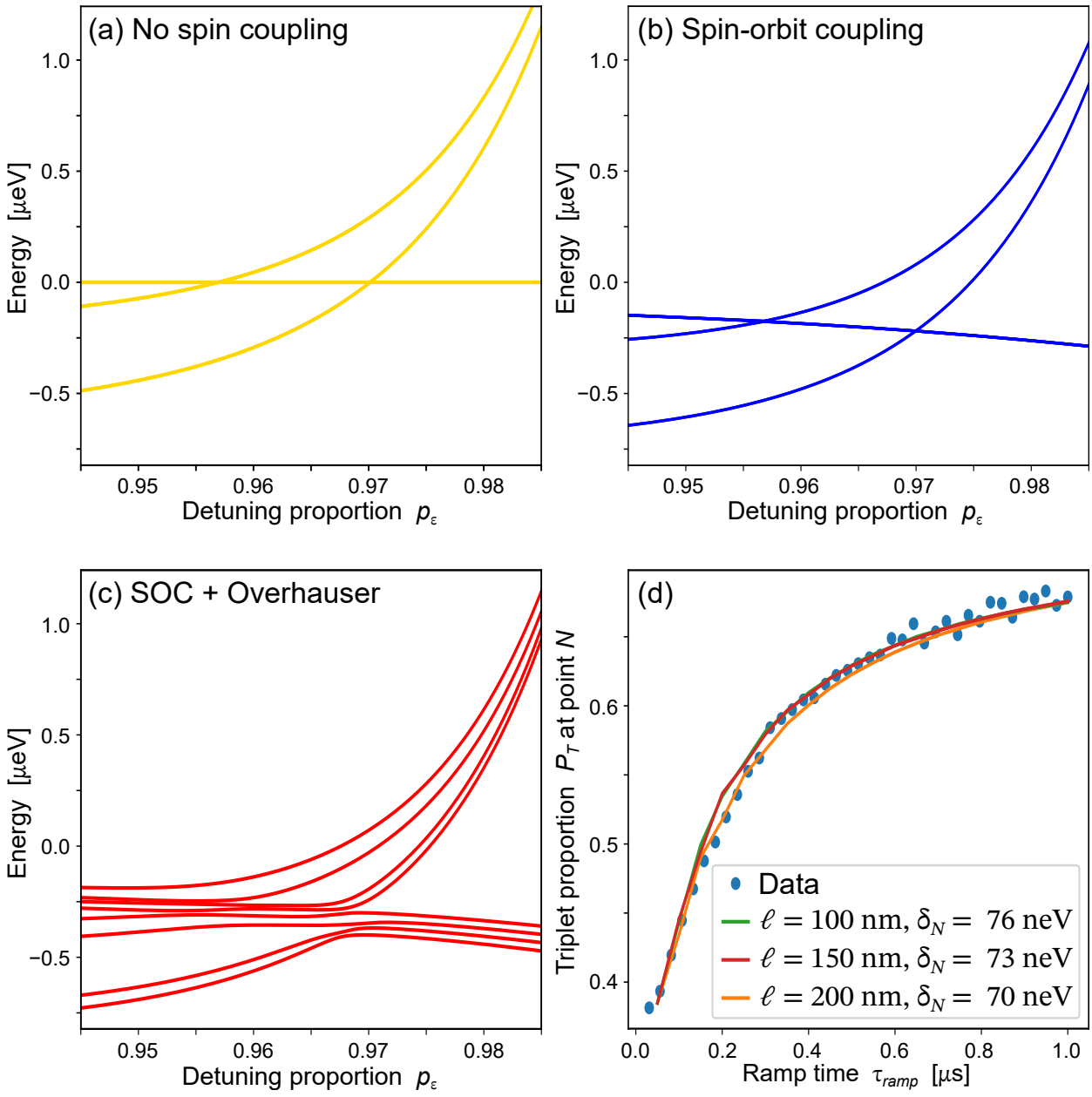

FIG. S2. (a)-(c) Calculated spectra of the experimental system as function of detuning proportion, comparing the effects of different mechanisms for spin coupling: (a) spectrum without any spin coupling effects; (b) spectrum including spin-orbit coupling effects calculated for this system as described in the supplementary text; (c) Sample spectrum with both spin-orbit and hyperfine induced Overhauser field gradients, using a single combination of h_{Na} fields selected from a normal distribution with standard deviation $\delta_N = 73$ neV. (d) Fits to the experimental data from Fig. 3b, using the time evolution simulations described in the supplementary text, for different values of distance between neighboring dots.

Time evolution simulations

Using the full Hamiltonian with spin-coupling, we perform time evolution calculations to simulate the conditions in the p_ϵ pulsing experiments. In the experiment, we initialize the ground state at point M and ramp adiabatically to $p_\epsilon = 0.8$, before pulsing to point N with a variable ramp time τ_{ramp}.

We use an in-house solver package [S1] to simulate the evolution of the initialized state for the last 20% of p_ϵ with varying ramp times. At $p_\epsilon = 0.8$, we consider the initialized state as a statistical mixture of the two lowest energy eigenstates, both of which are $s = 1/2$ states at $p_\epsilon = 0.8$. We consider 20 values of τ_{ramp} in the range from 50 ns

to 1 μs, taking 10000 time-steps for each ramp. We then add the overlaps of the averaged density matrix with each of the four lowest energy eigenstates at point N (i.e., the eigenstates with $s = 3/2$). This overlap can be mapped to an ideal P_T measurement with the method described two sections below. For each value of τ_{ramp}, we repeat the evolution 350 times, drawing different values of h_{Na}, and compute the average P_T for the final state. To account for imperfections of the experimental measurement of P_T–caused by the finite measurement bandwidth, the signal to noise ratio and $|T\rangle$ to $|S\rangle$ relaxation, as well as unwanted leakage to other states during the pulsed passages–we scale the ideal calculated values of $P_T(\tau_{ramp})$ to match the experimental P_T at the minimum and maximum value of τ_{ramp}.

We vary the parameter δ_N and use the method above to get the best fit to our experimental data. Additionally, the spin-orbit term requires an estimate of the distance between neighboring dots, which was lithographically designed to be $\ell = 150$ nm. We consider a conservative range of ℓ from 100 to 200 nm (see Fig. S2d), from which we extract the estimate for $\delta_N = 73 \pm 3$ neV quoted in the main text.

Extracting δ_N from the Landau-Zener model

The nuclear fields lead to the lifting of the spin degeneracies of the $s = 3/2$ quadruplet and the $s = 1/2$ doublets and multiple avoided crossings of the order of δ_N. A simple estimate of the characteristic time-scale of crossover between the diabatic and the adiabatic regimes of voltage tuning can be obtained by using the Landau-Zener formula for a two-level system [S2]. Then the characteristic ramp time is

$$\tau^*_{ramp} = \frac{\hbar \Delta p_\epsilon}{2\pi \delta_N^2} \frac{d\Delta E}{dp_\epsilon}. \tag{S19}$$

For $\Delta p_\epsilon = 0.2$ this gives $\tau^*_{ramp} \sim 100\,\text{ns}$, which is consistent with the time scale obtained by the time-dependent numerical simulation of the model.

External magnetic field

To capture the orbitals effects resulting from a magnetic flux through the square plaquette, we modify the tunneling term in Eq. S11 as $-\sum_{\langle j,k\rangle\sigma} t_{jk} e^{-i\varphi_{jk}} c^\dagger_{j\sigma} c_{k\sigma}$, with the Peierls phase:

$$\varphi_{jk} = \frac{e}{\hbar} \int_{\mathbf{r}_k}^{\mathbf{r}_j} d\mathbf{r} \cdot \mathbf{A}(\mathbf{r}) = \frac{2\pi}{\Phi_0} \int_{\mathbf{r}_k}^{\mathbf{r}_j} d\mathbf{r} \cdot \mathbf{A}(\mathbf{r}), \tag{S20}$$

where $e > 0$ is the elementary charge, $\hbar$ is the reduced Planck constant, $\Phi_0 = h/e$ is the flux quantum, and $\mathbf{A}(\mathbf{r})$ is the magnetic vector potential. We use the gauge for which $\varphi_{41} = 2\pi\Phi/\Phi_0$, with $\Phi = B\ell^2$ the magnetic flux through the plaquette and ℓ the length of the side of the plaquette, and the phases for the other links vanish.

The Zeeman contribution is:

$$\mathcal{H}_Z = g\mu_B \mathbf{B} \cdot \mathbf{S}, \tag{S21}$$

where $\mathbf{B}$ is the external magnetic field.

Charge stability simulations

In this work we use charge stability diagrams to identify different charge occupation regimes and charge transitions as function of gate voltages. To accurately simulate the charge stability diagrams, we modify our model to expand the number of basis states such that the system is no longer constrained to a total of 3 electrons, while each dot can still be occupied by 0 to 2 electrons, and we include the effect of intersite Coulomb repulsion, by adding a $\sum_{i<j} V_{i,j} n_i n_j$ term to Eq. S11. Additionally, we use gate to local energy lever arms and a cross-capacitance matrix measured from experiment to implement gate voltages P_i into the model and calculate their effect on local energies μ_i. We use this model to calculate charge occupation as a function of gate voltages. We used the simulation toolbox in the Python based package *qtt* [S5] to run these simulations.

AB INITIO EXACT DIAGONALIZATION SIMULATIONS OF THE 2×2 PLAQUETTE

We have developed an ab initio model of the quantum dot plaquette used in the experiments, in order to provide, in some aspects, more realistic benchmarks than the single-band Hubbard model used throughout. The model employs the eigenstate wavefunctions of a single Gaussian quantum well $V(\mathbf{r}) = -V_0 e^{-|\mathbf{r}|^2/2\delta}$ as the basis, and expands the tight-binding parameters on their Wannier orbitals. Taking the second quantization of the Wannier orbitals, the quadratic part of the Hamiltonian is

$$h_{i\alpha,j\beta} = \langle i\alpha\sigma|\mathcal{H}|j\beta\sigma\rangle, \tag{S22}$$

where $h_{i\alpha,j\beta}$ define the site energy (diagonal terms) and hybridization (off-diagonal terms) of the Wannier orbitals, for dot centers $\{i, j\}$, and orbital and spin indexes $\{\alpha, \beta\}$ and σ respectively. The on-site interactions are computed after formulating an on-site multiplet model [S6]:

$$\mathcal{H}_i^{(\mathrm{int})} = \frac{1}{2}\sum_{\alpha\sigma} U_\alpha n_{\alpha\bar{\sigma}} n_{\alpha\sigma} + \frac{1}{2}\sum_{\alpha_1\neq\alpha_2}\sum_{\sigma_1,\sigma_2} U'_{\alpha_1\alpha_2} n_{\alpha_2\sigma_2} n_{\alpha_1\sigma_1} + \frac{1}{2}\sum_{\alpha_1\neq\alpha_2}\sum_{\sigma_1,\sigma_2} J_{\alpha_1\alpha_2} c^\dagger_{\alpha_2\sigma_1} c^\dagger_{\alpha_1\sigma_2} c_{\alpha_2\sigma_2} c_{\alpha_1\sigma_1}, \tag{S23}$$

where U is the Coulomb repulsion between electrons on the same orbital (i.e., the on-site Hubbard interaction), U' is the inter-orbital Coulomb repulsion and J is the exchange interaction between spins on different orbitals (i.e., the Hund exchange). Similarly, through two-center integrals, we decompose the long-range interaction into:

$$\begin{aligned}\mathcal{H}_{ij}^{(\mathrm{int})} = &\frac{1}{2}\sum_{\alpha\sigma}\sum_{\beta\sigma'} V_{\alpha\beta} n_{i\alpha\sigma} n_{j\beta\sigma'} + \frac{1}{2}\sum_{\alpha\beta}\sum_{\sigma\sigma'} K_{\alpha\beta} c^\dagger_{j\beta\sigma} c^\dagger_{i\alpha\sigma'} c_{j\beta\sigma'} c_{i\alpha\sigma} \\ &+ \frac{1}{2}\sum_{\alpha\neq\beta}\sum_{\sigma\sigma'} V'_{\alpha\beta} c^\dagger_{i\beta\sigma} c^\dagger_{j\alpha\sigma'} c_{j\beta\sigma'} c_{i\alpha\sigma} + \frac{1}{2}\sum_{\alpha\neq\beta}\sum_{\sigma\sigma'} K'_{\alpha\beta} c^\dagger_{j\alpha\sigma} c^\dagger_{i\beta\sigma'} c_{j\beta\sigma'} c_{i\alpha\sigma},\end{aligned} \tag{S24}$$

where $V_{\alpha\beta}$ represents the Coulomb interaction and $K_{\alpha\beta}$ is the corresponding exchange interaction; similarly, $V'_{\alpha\beta}$ is the correlation between two on-site exchange interactions, while $K'_{\alpha\beta}$ is the correlation between off-site exchange.

Modeling of the experimental device

We set the variance of the quantum well potential $\delta = 100$ nm equal to the designed diameter of the quantum dots in the device [23]. Setting the potential depth $V_0 = 11.4$ meV, we obtain the first-excited-state level spacing $\varepsilon_1 - \varepsilon_0 \approx 0.75$ meV. The evaluation of the electron-electron interaction requires a specific value of the dielectric constant, whose bulk value is $\epsilon = 12.9$ in GaAs. However, since the gate electrodes contribute an additional capacitance to the self-capacitance between the dot and the reservoir, we can account for this effect by selecting a larger effective ϵ. Using $\epsilon = 20$ in the quantum-dot system mentioned above, we obtain the ground-state Hubbard interaction $U_0 \approx 2.34$ meV and the ground-excited-state interaction $U'_{01} \approx 1.92$ meV. This makes the model consistent with the experimental measurements. This multi-orbital ab initio model correctly captures the energy level mixture caused by having the on-site interaction being much larger than the orbital energy-level spacing, a feature that is characteristic of quantum dots.

We calculate the long-range interactions for a distance $d = 210$ nm between neighboring dots in the plaquette. The Coulomb interaction V obtained from calculation ranges from 0.22 meV to 0.4 meV depending on the orbitals, K and V' are on the order of or below 1 μeV, and K' is even lower, on the order of 0.1 or 0.01 μeV. Even though these higher-order correction terms are much smaller than the on-site interactions, they are still comparable to the ~ 1 μeV high-spin to low-spin energy gap–which we refer to as the Nagaoka gap–and should be taken into account.

For clarity, we distinguish between the *hopping parameter* in the ab initio model, and the experimentally measured *tunnel coupling*. Different from the single-band model described in the previous section, the hopping strength has contributions from all possible paths through different orbitals. The hopping parameters in the tight-binding model vary among different orbitals and typically decrease exponentially as a function of the distance between quantum wells. Since the ground-state wavefunction is most localized, hybridization between two ground states across neighboring quantum wells is small (~ 0.06 μeV for $d = 210$ nm). However, with the presence of multiple quantum dots, there is strong hybridization between the ground state and local excited states (the maximum of which can be close to the energy level spacing). These high-level excited states can contribute a ~ 0.5 meV hopping strength. Therefore, the tunnel couplings among low-energy states of neighboring quantum wells–obtained from the superposition of all contributing paths–become much larger than the bare hopping parameter between ground states (the latter is

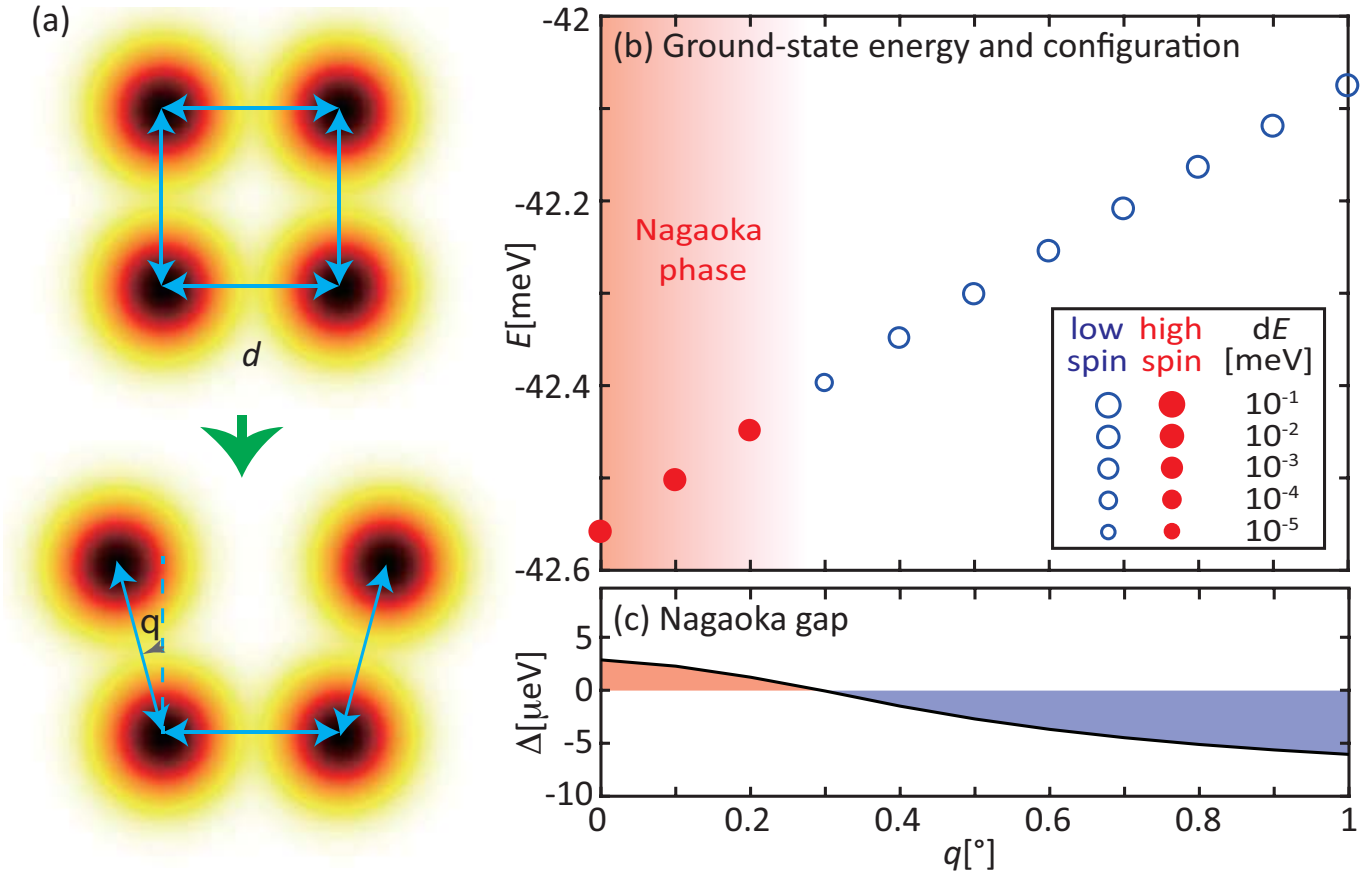

FIG. S3. (a) Schematic of the methodology used in the ab initio simulations to reproduce the effect of the 4-dot system transition from a 2D plaquette to a 1D chain. We gradually vary the angle θ, which effectively varies the distance between two of the dots. (b) The ground-state energy and spin configuration, and (c) the high-spin to low-spin energy gap as a function of θ. The ground state soon becomes a low-spin state for the rotating angle at 0.3°.

$\sim 0.06\mu$eV). In our ab initio calculation, we estimate the tunnel coupling t by calculating the single-particle bandwidth in the system. Assuming t is dominated by nearest-neighbor tunneling, the low-energy band structure of a 2×2 plaquette is $-2t\cos\theta$ where θ goes from 0 to 2π. Therefore, the width of the lowest single-electron band (the lowest four states) is approximately $4t$. For our chosen $d = 210$ nm, the model predicts $t \approx 40$ μeV, similar to the values measured in the experiment.

We perform the ab initio, exact-diagonalization calculation, with three electrons in a four-well system, emulating the experimental conditions. The bottom-level differential equation and integration are calculated on a grid with a spacing of 1nm. To simplify the calculation, we keep 15 orbitals in each quantum well, which span a ~ 5 meV energy range, much larger than both U and t. The solution indeed predicts a high-spin ground state, with a Nagaoka gap of ~ 3 μeV.

We have reproduced two of the experiments described in the main text. We first model the transition of the 4-dot array from a ring to a chain, by gradually increasing the distance between two of the dots Fig. S3. This effectively reduces the tunneling term between them, with a transition to a low-spin ground state as the system becomes more 1D-like, as described in the main text.

Finally, we reproduced the effect of varying the local energy offset, by gradually varying the amplitude of the potential of the quantum well in one of the dots Fig. S4. The model predicts transitions to a low-spin ground state for both positive and negative local offsets. As observed in the experiment, these transitions occur over a range of energy orders of magnitude larger than the tunnel coupling, and with a similar asymmetry between positive and negative offsets.

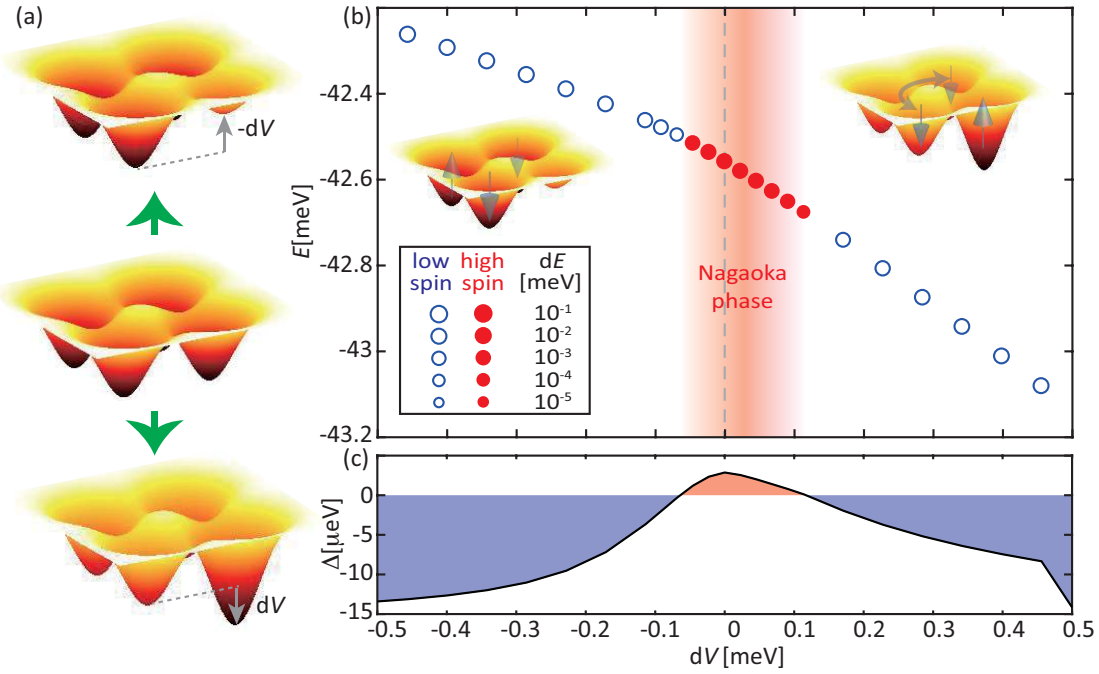

FIG. S4. (a) Schematic of the methodology used in the ab initio simulations to reproduce the effect of a local energy offset. The amplitude of the potential of one of the quantum wells is changed by an amount dV. The variation of the single-well potential by positive or negative dV gives unbalanced site-energies. Besides, with the change of eigenstate basis, the hybridization and interaction parameters are also affected in the ab initio calculation. (b) The ground-state energy and spin configuration, and (c) the high-spin to low-spin energy gap as a function of dV. When the potential detuning is $dV = 0.11$ meV or $dV = -0.07$ meV, the system undergoes a transition to a low-spin ground state. The transitions at these two directions have a different nature, as drawn in the insets. For $dV > 0$, the particular quantum dot is deeper and tends to trap more electrons. On the other hand, a negative dV raises the energy cost on the particular quantum well and leads to a lower probability of occupation in a three-electron system. Without the "mobile" hole in the "half-filled" system, the ground state becomes a low-spin state instead a Nagaoka ferromagnetic state.

MAPPING 3-SPIN STATES ONTO 2-SPIN MEASUREMENTS

In the main text, we state that we can distinguish between the 3-spin $s = 1/2$ and $s = 3/2$ states through a projective singlet/triplet ($|S\rangle/|T\rangle$) measurement on 2 random spins. Here we show this in the first-quantization formulation of the spin states. We use the following 8 basis states of the system with 3 spin-$\frac{1}{2}$ particles:

$$
\begin{aligned}
|\tfrac{3}{2},+\tfrac{3}{2}\rangle &= |\uparrow\uparrow\uparrow\rangle \\
|\tfrac{3}{2},+\tfrac{1}{2}\rangle &= \frac{1}{\sqrt{3}}\left(|\uparrow\uparrow\downarrow\rangle + |\uparrow\downarrow\uparrow\rangle + |\downarrow\uparrow\uparrow\rangle\right) \\
|\tfrac{3}{2},-\tfrac{1}{2}\rangle &= \frac{1}{\sqrt{3}}\left(|\downarrow\downarrow\uparrow\rangle + |\downarrow\uparrow\downarrow\rangle + |\uparrow\downarrow\downarrow\rangle\right) \\
|\tfrac{3}{2},-\tfrac{3}{2}\rangle &= |\downarrow\downarrow\downarrow\rangle \\
|\tfrac{1}{2},+\tfrac{1}{2}\rangle_1 &= \frac{1}{\sqrt{3}}\left(-|\uparrow\uparrow\downarrow\rangle + e^{i\pi/3}|\uparrow\downarrow\uparrow\rangle + e^{-i\pi/3}|\downarrow\uparrow\uparrow\rangle\right) \\
|\tfrac{1}{2},-\tfrac{1}{2}\rangle_1 &= \frac{1}{\sqrt{3}}\left(-|\downarrow\downarrow\uparrow\rangle + e^{i\pi/3}|\downarrow\uparrow\downarrow\rangle + e^{-i\pi/3}|\uparrow\downarrow\downarrow\rangle\right) \\
|\tfrac{1}{2},+\tfrac{1}{2}\rangle_2 &= \frac{1}{\sqrt{3}}\left(-|\uparrow\uparrow\downarrow\rangle + e^{-i\pi/3}|\uparrow\downarrow\uparrow\rangle + e^{i\pi/3}|\downarrow\uparrow\uparrow\rangle\right) \\
|\tfrac{1}{2},-\tfrac{1}{2}\rangle_2 &= \frac{1}{\sqrt{3}}\left(-|\downarrow\downarrow\uparrow\rangle + e^{-i\pi/3}|\downarrow\uparrow\downarrow\rangle + e^{i\pi/3}|\uparrow\downarrow\downarrow\rangle\right)
\end{aligned}
\tag{S25}
$$

The 2-spin system has one singlet ($|S\rangle$) and three triplet states ($|T_+\rangle, |T_0\rangle, |T_-\rangle$), given by:

$$\begin{aligned}
|S\rangle &= |0,0\rangle = \frac{1}{\sqrt{2}}\left(|\uparrow\downarrow\rangle - |\downarrow\uparrow\rangle\right) \\
|T_+\rangle &= |1,+1\rangle = |\uparrow\uparrow\rangle \\
|T_0\rangle &= |1,0\rangle = \frac{1}{\sqrt{2}}\left(|\uparrow\downarrow\rangle + |\downarrow\uparrow\rangle\right) \\
|T_-\rangle &= |1,-1\rangle = |\downarrow\downarrow\rangle
\end{aligned} \tag{S26}$$

To obtain the 2-spin projection on the 3-spin system, we take partial inner products of each of the eight basis states with singlet and triplet states in the first two spins. First, we take the basis state $|\frac{3}{2},+\frac{3}{2}\rangle$:

$$\begin{aligned}
\langle S|\frac{3}{2},+\frac{3}{2}\rangle &= \frac{1}{\sqrt{2}}\left[\langle\uparrow\downarrow| - \langle\downarrow\uparrow|\right]\left[|\uparrow\uparrow\uparrow\rangle\right] = 0 \\
\langle T_0|\frac{3}{2},+\frac{3}{2}\rangle &= \frac{1}{\sqrt{2}}\left[\langle\uparrow\downarrow| + \langle\downarrow\uparrow|\right]\left[|\uparrow\uparrow\uparrow\rangle\right] = 0 \\
\langle T_+|\frac{3}{2},+\frac{3}{2}\rangle &= \langle\uparrow\uparrow\,|\,\uparrow\uparrow\uparrow\rangle = |\uparrow\rangle \\
\langle T_+|\frac{3}{2},+\frac{3}{2}\rangle &= \langle\downarrow\downarrow\,|\,\uparrow\uparrow\uparrow\rangle = 0
\end{aligned} \tag{S27}$$

The probability of $|S\rangle$ and $|T\rangle$ measurement outcomes in 2-spin projective measurements of the $|\frac{3}{2},+\frac{3}{2}\rangle$ basis state are

$$\|\langle S|\frac{3}{2},+\frac{3}{2}\rangle\|^2 = 0 \quad \text{and} \quad \|\langle T_+|\frac{3}{2},+\frac{3}{2}\rangle\|^2 + \|\langle T_0|\frac{3}{2},+\frac{3}{2}\rangle\|^2 + \|\langle T_-|\frac{3}{2},+\frac{3}{2}\rangle\|^2 = 1+0+0 = 1.$$

Following similar derivations, we find that also for the other three basis states with $s = 3/2$, the probabilities of obtaining $|S\rangle$ and $|T\rangle$ upon measurement are 0 and 1 respectively.

Next, we take the basis state $|\frac{1}{2},+\frac{1}{2}\rangle_1$:

$$\begin{aligned}
\langle S|\frac{1}{2},+\frac{1}{2}\rangle_1 &= \frac{1}{\sqrt{2}}\left[\langle\uparrow\downarrow| - \langle\downarrow\uparrow|\right]\frac{1}{\sqrt{3}}\left[-|\uparrow\uparrow\downarrow\rangle + e^{i\pi/3}|\uparrow\downarrow\uparrow\rangle + e^{-i\pi/3}|\downarrow\uparrow\uparrow\rangle\right] \\
&= \frac{1}{\sqrt{6}}\left[e^{i\pi/3} - e^{-i\pi/3}\right]|\uparrow\rangle = \frac{i}{\sqrt{2}}|\uparrow\rangle \\
\langle T_0|\frac{1}{2},+\frac{1}{2}\rangle_1 &= \frac{1}{\sqrt{2}}\left[\langle\uparrow\downarrow| + \langle\downarrow\uparrow|\right]\frac{1}{\sqrt{3}}\left[-|\uparrow\uparrow\downarrow\rangle + e^{i\pi/3}|\uparrow\downarrow\uparrow\rangle + e^{-i\pi/3}|\downarrow\uparrow\uparrow\rangle\right] \\
&= \frac{1}{\sqrt{6}}\left[e^{i\pi/3} + e^{-i\pi/3}\right]|\uparrow\rangle = \frac{1}{\sqrt{6}}|\uparrow\rangle \\
\langle T_+|\frac{1}{2},+\frac{1}{2}|_\rangle 1 &= \langle\uparrow\uparrow|\frac{1}{\sqrt{3}}\left[-|\uparrow\uparrow\downarrow\rangle + e^{i\pi/3}|\uparrow\downarrow\uparrow\rangle + e^{-i\pi/3}|\downarrow\uparrow\uparrow\rangle\right] = -\frac{1}{\sqrt{3}}|\downarrow\rangle \\
\langle T_-|\frac{1}{2},+\frac{1}{2}\rangle_1 &= \langle\downarrow\downarrow|\frac{1}{\sqrt{3}}\left[-|\uparrow\uparrow\downarrow\rangle + e^{i\pi/3}|\uparrow\downarrow\uparrow\rangle + e^{-i\pi/3}|\downarrow\uparrow\uparrow\rangle\right] = 0
\end{aligned} \tag{S28}$$

This results in 2-spin measurement probabilities of:

$$\|\langle S|\frac{1}{2},+\frac{1}{2}\rangle_1\|^2 = \frac{1}{2} \quad \text{and} \quad \|\langle T_+|\frac{1}{2},+\frac{1}{2}\rangle_1\|^2 + \|\langle T_0|\frac{1}{2},+\frac{1}{2}\rangle_1\|^2 + \|\langle T_-|\frac{1}{2},+\frac{1}{2}\rangle_1\|^2 = \frac{1}{3}+\frac{1}{6}+0 = \frac{1}{2}.$$

Similar calculations for the other three basis states with $s = 1/2$ show $|S\rangle$ and $|T\rangle$ measurement probabilities of 0.5 each. Although we have used the 2 spin singlet and triplet states for the first two spins for the calculations, same results hold for any other two spin combinations.

Assuming statistical mixing of the 8 basis states with 3 spin-1/2 particles, the probability of a two-spin singlet measurement outcome is given by:

$$P_S = \sum_{s,m} P(s,m)||\langle S|s,m\rangle||^2$$

where $P(s,m)$ is the probability of occupation of the three-electron spin state $|s,m\rangle$. Similarly the probability of a two-spin triplet measurement outcome is given by:

$$P_T = \sum_{s,m} P(s,m)\left[||\langle T_+|s,m\rangle||^2 + ||\langle T_0|s,m\rangle||^2 + ||\langle T_-|s,m\rangle||^2\right]$$

As we have seen before, for any basis state with $s = 3/2$, the probability two-spin triplet measurement outcome is 1. So, for any statistical mixture of $s = 3/2$ basis states, the probability a two-spin triplet measurement outcome is also 1. Similarly, for any statistical mixture of $s = 1/2$ basis states, the probability a two-spin triplet measurement outcome is 0.5. So in our experiment the expected values of $P_T^{3/2}$ and $P_T^{1/2}$ are 1 and 0.5, where $P_T^{3/2}$ ($P_T^{1/2}$) is the probability a two-electron triplet state measurement outcome from the quadruplet (doublet) configuration.

[S1] https://github.com/stephanlphilips/dm_solver.
[S2] L. D. L. Landau and E. M. Lifshitz, *Quantum Mechanics* (Elsevier Science, 2013).
[S3] D. Stepanenko, M. Rudner, B. I. Halperin, and D. Loss, Phys. Rev. B **85**, 075416 (2012).
[S4] R. Winkler, *Spin–orbit coupling effects in two-dimensional electron and hole systems* (Springer Berlin Heidelberg, 2003).
[S5] https://github.com/QuTech-Delft/qtt.
[S6] E. Dagotto, *Nanoscale Phase Separation and Colossal Magnetoresistance* (Springer Berlin Heidelberg, 2003).

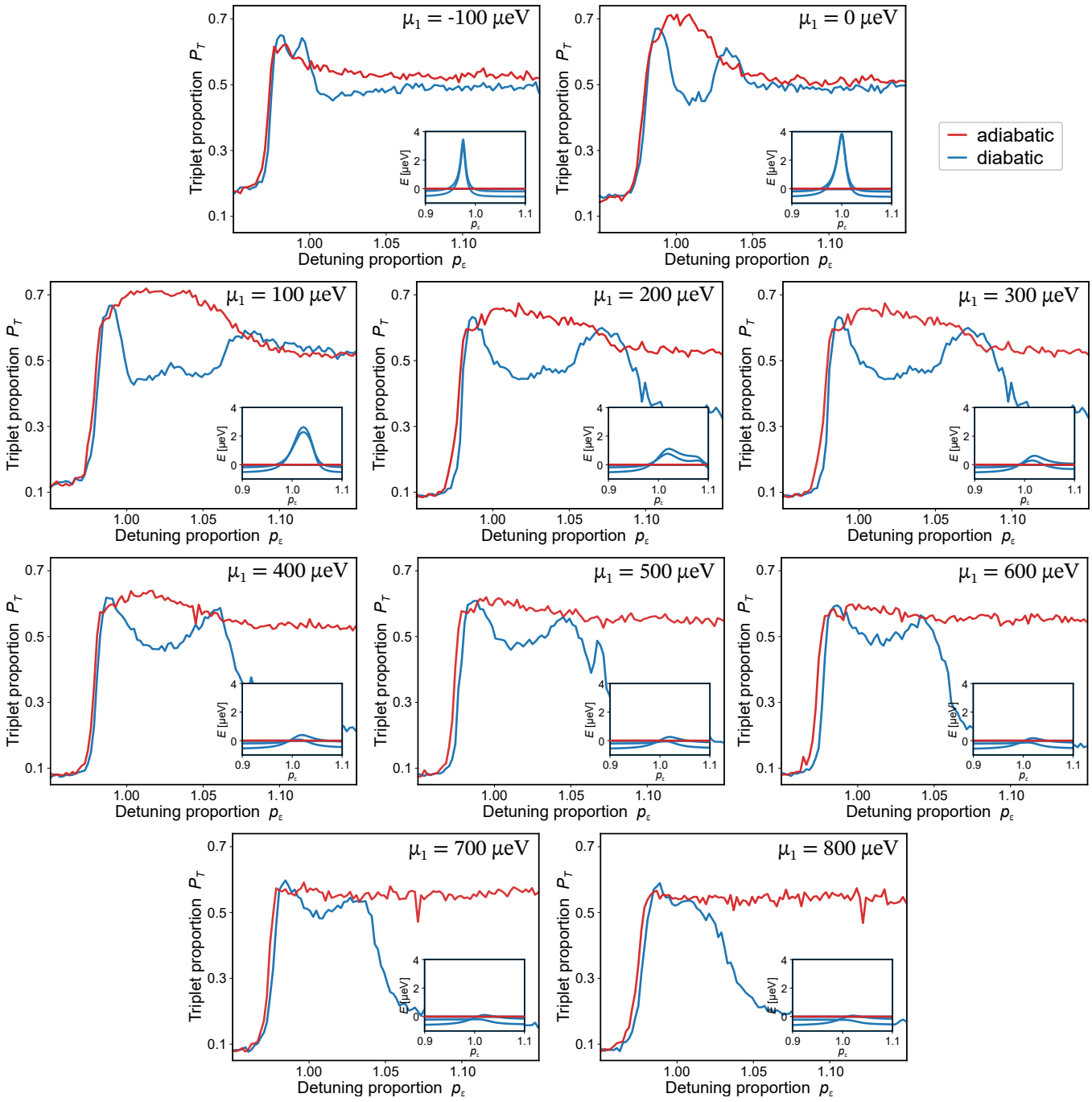

FIG. S5. Each panel experimental measurements comparing adiabatic and diabatic passages (as explained in the main text), where point N has been redefined such that the chemical potential of dot 1 is offset by the amount shown on the top right of each panel. Insets show simulated spectra using the same local offset conditions as the experiment of the corresponding panel.